Universiteit Leiden
The Netherlands

The roles of morphology and environment on the star formation rate-stellar mass relation in COSMOS from 0 < z < 3.5

Cooke, K.C.; Kartaltepe, J.S.; Rose, C.; Tyler, K.D.; Darvish, B.; Leslie, S.K.; ... ; Koekemoer, A.M.

The Roles of Morphology and Environment on the Star Formation Rate–Stellar Mass Relation in COSMOS from $0 < z < 3.5$

Kevin C. Cooke[1,2,3] , Jeyhan S. Kartaltepe[3] , Caitlin Rose[3] , K. D. Tyler[3], Behnam Darvish[4] , Sarah K. Leslie[5] ,
Ying-jie Peng[6], Boris Häußler[7], and Anton M. Koekemoer[8]

[1] AAAS S&T Policy Fellow hosted at the National Science Foundation, 1200 New York Ave, NW, Washington, DC 20005, USA; astrokevincooke@gmail.com
[2] Department of Physics & Astronomy, University of Kansas, Lawrence, KS 66045, USA
[3] Laboratory for Multiwavelength Astrophysics, School of Physics and Astronomy, Rochester Institute of Technology, Rochester, NY 14623, USA
jeyhan@astro.rit.edu
[4] Cahill Center for Astrophysics, California Institute of Technology, 1216 East California Boulevard, Pasadena, CA 91125, USA
[5] Leiden Observatory, Leiden University, PO Box 9513, NL-2300 RA Leiden, Netherlands
[6] Kavli Institute for Astronomy and Astrophysics (KIAA), Peking University, Beijing 100871, People's Republic of China
[7] European Southern Observatory, Alonso de Cordova 3107, Vitacura, Casilla 19001, Santiago, Chile
[8] Space Telescope Science Institute, 3700 San Martin Dr., Baltimore, MD, 21218, USA

Abstract

We investigate the relationship between environment, morphology, and the star formation rate (SFR)–stellar mass relation derived from a sample of star-forming (SF) galaxies (commonly referred to as the "star formation main sequence", SFMS) in the COSMOS field from $0 < z < 3.5$. We constructed and fit the far-UV–far-IR spectral energy distributions of our stellar-mass-selected sample of 111,537 galaxies with stellar and dust emission models using the public packages MAGPHYS and SED3FIT. From the best-fit parameter estimates, we construct the SFR–stellar mass relation as a function of redshift, local environment, NUVrJ color diagnostics, and morphology. We find that the shape of the main sequence derived from our color–color and specific-star-formation-rate-selected SF galaxy population, including the turnover at high stellar mass, does not exhibit an environmental dependence at any redshift from $0 < z < 3.5$. We investigate the role of morphology in the high-mass end of the SFMS to determine whether bulge growth is driving the high-mass turnover. We find that SF galaxies experience this turnover independent of bulge-to-total ratio, strengthening the case that the turnover is due to the disk component's specific SFR evolving with stellar mass rather than bulge growth.

1. Introduction

Toward the goal of understanding the star formation history of today's galaxy population, many surveys have studied the tight correlation between the star formation rate (SFR) and stellar mass (M_*) of star-forming (SF) galaxies over cosmic time. Such surveys have found a relatively low dispersion correlation, known by many names such as the star formation main sequence, the star-forming main sequence, the galaxy main sequence, and the SFR–stellar mass relation (e.g., Brinchmann et al. 2004; Daddi et al. 2007; Elbaz et al. 2007; Noeske et al. 2007; Salim et al. 2007; Pannella et al. 2009; Magdis et al. 2010; Rodighiero et al. 2010; Wuyts et al. 2011; Whitaker et al. 2012; Schreiber et al. 2015; Leslie et al. 2020). Due to its wide use, we will refer to this trend as the star formation main sequence (SFMS).

The SFMS relation is an indication that the SF galaxy population spends a significant amount of its lifetime forming stars at a roughly steady state correlated with its stellar mass, and any deviations in star formation are short lived until the galaxy is finally quenched, dropping off the SFMS. Galaxies with SFRs significantly above the SFMS ($>3 \times$ SFMS) are often classified as "starbursts," with intense star formation triggered through secular processes and/or mergers (e.g.,

Kartaltepe et al. 2012; Hung et al. 2013; Willett et al. 2015). Galaxies below the SFMS predominantly lie in a cloud of "passive galaxies" exhibiting SFRs an order of magnitude or more below the SFMS (e.g., Morselli et al. 2019). Between the SFMS and the quiescent population, in a region dubbed the "green valley," lie an intermediate group of galaxies experiencing a temporary lull or the in-progress quenching of their star formation (Strateva et al. 2001; Baldry et al. 2004, 2006), or are experiencing rejuvenation (Chauke et al. 2019; Mancini et al. 2019). With rising redshift comes a rising normalization (Noeske et al. 2007; Whitaker et al. 2012; Rodighiero et al. 2014; Johnston et al. 2015; Lee et al. 2015), reaching its maximum normalization at cosmic noon ($z \sim 2$; Madau & Dickinson 2014). This rising normalization is consistent with the higher gas masses of galaxies in the early universe across several decades in stellar mass (Magdis et al. 2012; Genzel et al. 2015; Schinnerer et al. 2016; Scoville et al. 2016; Liu et al. 2019).

The shape of the SFMS at $z > 1$ is roughly consistent with low-redshift samples (e.g., Whitaker et al. 2012; Lee et al. 2015), however several questions remain at the high-mass end. At stellar masses $>10^{10} M_\odot$ there is a debated turnover in the shape of the SFMS, where progressively higher masses no longer correspond to higher SFRs. Recent work found the degree of the turnover is reduced when only considering disk-dominated, or the disk components of, SF galaxies (Abramson et al. 2014; Guo et al. 2015). This was interpreted as an indication that the turnover at high mass is due to the growth of

the quiescent bulge component and the SF disk components form stars at a consistent level independent of bulge mass. However, this behavior is contested by studies that find the turnover remains when considering the SFR of disks (Schreiber et al. 2016; Catalán-Torrecilla et al. 2017; Morselli et al. 2017; Belfiore et al. 2018; Cook et al. 2020). Other studies have alternatively interpreted the turnover as a reduction in the star formation per unit stellar mass (specific star formation rate, sSFR; Whitaker et al. 2012, 2014; Lee et al. 2015; Tomczak et al. 2016; Lee et al. 2018). Further complicating matters is recent work examining this behavior on an individual SF region basis for local galaxies, where Atacama Large Millimeter/submillimeter Array observations find an incredible galaxy-to-galaxy variation in star formation efficiency at the highest SF clump stellar masses (Ellison et al. 2021). The disagreement between results which observe a turnover in SF galaxies' disk components (e.g., Belfiore et al. 2018; Cook et al. 2020), and those that do not (e.g., Abramson et al. 2014; Guo et al. 2015) motivate us to determine how the SFMS may change with respect to different morphology-selected samples.

While the role of morphology in the high-mass turnover remains under investigation, there are additional questions regarding the role of local environment (i.e., the galaxy number density in the immediate vicinity of a given galaxy) on the shape of the SFMS. At low redshift, there is a morphology–density relation where quiescent, spheroidal galaxies more commonly inhabit dense environments while star-forming, disk-like galaxies more commonly inhabit the field (e.g., Dressler 1980; Lin et al. 2014; Erfanianfar et al. 2015). This environmental dependence is thought to be due to the removal of cold gas in satellite galaxies after interacting with the warm intracluster medium of the host cluster (Gunn et al. 1972). As the SFMS is estimated using SF galaxies, the shape of the SFMS is dominated by star-forming, disk field galaxies at low redshift. Thus, measuring the shape of the SFMS across different environments is required to understand whether environment plays a role in the global turnover at high mass.

The role of the local environment on the shape of the SFMS becomes uncertain at high redshift ($z > 1$). Initially, an inversion of the relation between SFR and local density was observed at $z \sim 1$ (Elbaz et al. 2007; Cooper et al. 2008; Hilton et al. 2010; Santos et al. 2014), where higher density environments hosted increased SFRs or galaxies with higher total IR luminosity. The inversion was hypothesized to be due to the higher gas fractions present in early universe galaxies, enabling elevated levels of star formation in interaction-prone environments such as groups and protoclusters. However, some works have observed a flattening, but not quite an inversion, at $z > 1$ (Feruglio et al. 2010; Koyama et al. 2013; Scoville et al. 2013; Erfanianfar et al. 2015; Alberts et al. 2016; Hatfield & Jarvis 2017). The contrast between the observation of elevated SFRs in high-density regions, such as clusters, by some IR studies (e.g., Santos et al. 2014) and not others (e.g., Alberts et al. 2016) leads to the question of what trends can be deduced by a study that examines the local density surrounding SF galaxies across large cosmological volumes. Addressing this issue requires an understanding of the shape of the SFMS as a function of the environment, as well.

In this paper, we seek to estimate the roles of the morphology and local environment of SF galaxies on the SFMS using consistent methods across a larger span of redshift than examined in previous works that focused on either low- or

high-z samples. Previous works on tracing the SFMS across redshift (e.g., $z < 1.3$; Lee et al. 2015) were often limited to redshift ranges constrained by a given observation method's constraints, such as the redshifting out of the optical peak from individual filters. Additionally, some low-to-high redshift surveys were performed but did not include comparisons to both local environment and morphology (e.g., $0.2 < z < 2.5$, $0.2 < z < 6$, and $0 < z < 9$; Whitaker et al. 2014; Pearson et al. 2018; Thorne et al. 2021). Through the use of the k-corrected COSMOS2015 observations across the UV to far-IR (FIR), we investigate beyond the common stopping points near $z \sim 1$ to provide a point of comparison for high-z ($z < 3$) studies (Whitaker et al. 2014; Schreiber et al. 2015) in a self-consistent manner while considering how star formation correlates with local environment or morphology.

In Section 2 we describe our sample selection and the photometric and spectroscopic data set we use as input to the spectral energy distribution (SED) fitting packages described in Section 3. Our star formation–stellar mass relations are described in Section 4, and we consider their implications in Section 5. Finally, we review our findings in Section 6. This work assumes a Chabrier (2003) initial mass function (IMF) and the standard Lambda cold dark matter (ΛCDM) cosmological parameters $H_0 = 70$ Mpc^{-1} km s^{-1}, $\Omega_M = 0.3$, and $\Omega_{\mathrm{vac}} = 0.7$. All magnitudes are expressed in the AB magnitude system (Oke 1974).

2. Sample and Multiwavelength Data

We select our sample and corresponding photometric data from the public observations of the COSMOS field (Scoville et al. 2007). COSMOS is the largest contiguous area (2 sq. deg.) observed with the Hubble Space Telescope (HST), located at R. A. (J2000) = 10:00:28.600, decl. (J2000) = +02:12:21.00. We use the far-UV (FUV) to FIR data included in the COSMOS2015 catalog (Laigle et al. 2016) to construct SEDs and estimate galaxy stellar parameters for all galaxies above the stellar mass completeness limit from from $0 < z < 3.5$. We review the photometric data sources and properties below in Section 2.3; for greater detail, see Laigle et al. (2016). We apply galactic foreground corrections to photometry from the FUV-IRAC4 bands using a galactic reddening $R_v = 3.1$ (Morrissey et al. 2007) and $E(B-V)$ values from the dust maps of Schlegel et al. (1998).

2.1. Sample Selection

For our analysis, we require a mass complete sample across a wide redshift range. To ensure sample completeness across the full redshift range examined here, we select galaxies using the total stellar mass completeness limits from COSMOS2015 (Laigle et al. 2016). We plot our initial sample in Figure 1 with these stellar mass completeness limits. The Laigle et al. (2016) stellar mass limit was determined using the UltraVISTA Data Release 2 (DR-2) survey (McCracken et al. 2012) depths for the entire COSMOS field. To maintain sample completeness across the entire COSMOS field, we chose to use the shallower depth of UltraVISTA DR-2 rather than the depth of the UltraVISTA ultradeep strips of the center of the COSMOS field. We select galaxies from $0.0 < z < 3.5$ to probe both sides of the global star formation density peak of the universe (Madau & Dickinson 2014). Photometric redshifts from Laigle et al. (2016) were calculated using LePhare (Arnouts et al. 1999;
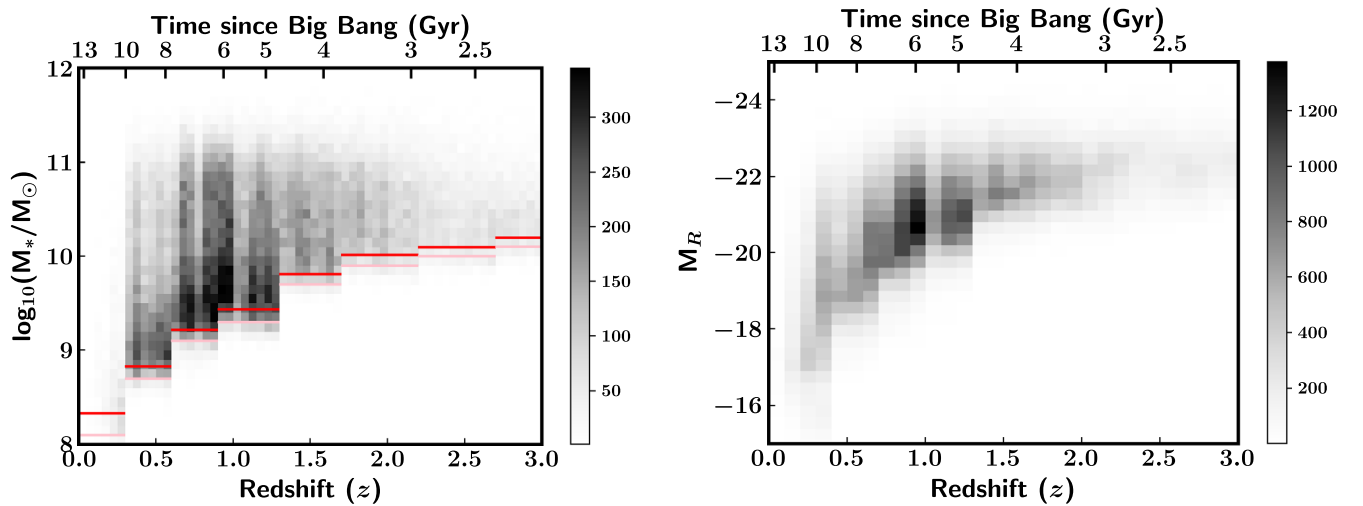
Figure 1. Left: the stellar mass distribution of our refit sample. The original Laigle et al. (2016) stellar mass completeness limits are in pink, and the completeness limits plus median stellar mass error are in red. Our analysis sample is selected from the completeness plus fitting error limit. Right: to enable reference to an observable quantity in parallel to SED-estimated stellar masses, we include the *k*-corrected M_r distribution of our sample with redshift.

Ilbert et al. 2006), yielding a photometric redshift accuracy of $1\sigma \sim 0.01$ at $z < 3$.

Our initial sample is only selected based on the COSMOS2015 stellar mass, with no consideration given to previously estimated SFRs, colors, or active galactic nucleus (AGN) activity. Our initial mass-selected sample from COSMOS2015 totaled 131,842 galaxies. We independently fit the SEDs of our sources because the COSMOS2015 catalog's original fit estimates presented in Laigle et al. (2016) prioritized photometric redshift and stellar mass determination by using only 12 Bruzual & Charlot (2003) templates for SF galaxies. To estimate SFRs with high accuracy, refitting with a higher number of models is desired for all objects. Additionally, the Laigle et al. (2016) fits only included photometry out to the 8 μm band of the Spitzer/Infrared Array Camera (IRAC) Channel 4 as input. This wavelength range restricts the original fit's capability to estimate obscured SFRs, and the resulting fits are primarily used for stellar mass selection of targets. To estimate SFRs inclusive of obscured and unobscured components, a fitting procedure with both mid-IR (MIR) and FIR points should be used.

As described in Section 3.1, we refit the SEDs of these targets to estimate accurate SFRs using the full range of IR data available and incorporating spectroscopic redshifts where available. To maintain the completeness of the sample, we use SED fits (described in Section 3.1) from galaxies with best-fit stellar masses above the Laigle completeness mass limit plus the median error of the best-fit SED stellar mass in a given redshift bin. This removes the parameter space where fits may scatter above or below the original completeness limit due to the refitting process. The final mass-selected sample used in our analysis totals 111,537 galaxies.

2.2. Spectroscopic Redshifts

Redshift quality plays a great importance in the constraining of stellar models for galaxies at all redshifts. After identifying our sample described in Section 2, we search the COSMOS spectroscopic catalog (M. Salvato et al. 2022, in preparation) for matches within $1''$ of the COSMOS2015 R.A. and decl. positions. Prior to SED fitting, we replace the photometric redshifts provided in the COSMOS2015 catalog with the matched spectroscopic redshifts from the following surveys

and observation campaigns: the 3D-HST Survey (Brammer et al. 2012; Momcheva et al. 2016), the DEIMOS 10K Spectroscopic Survey (Hasinger et al. 2018), the 2dF Galaxy Redshift Survey (Colless et al. 2001), the FMOS-COSMOS Survey (Kartaltepe et al. 2015; Silverman et al. 2015), the Gemini GMOS-S spectra of Balogh et al. (2011), the COSMOS Active Galactic Nucleus Spectroscopic Survey (Trump et al. 2007, 2009), the KMOS^{3D} Survey (Wisnioski et al. 2015), the AzTEC Millimeter Survey of the COSMOS Field (Scott et al. 2008), the 14th Data Release of the Sloan Digital Sky Survey (SDSS; Pâris et al. 2018), the Very Large Telescope LEGA-C Spectroscopic Survey (van der Wel et al. 2016), the ZFIRE KECK/MOSFIRE Spectroscopic Survey (Nanayakkara et al. 2016), the MOSFIRE Deep Evolution Field (MOSDEF) Survey (Kriek et al. 2015), the Keck LRIS spectra of Casey et al. (2017), the MOIRCS Deep Survey (Yoshikawa et al. 2010), the MMT/Hectoscec spectra of Trump et al. (2009), the Complete Calibration of the Color-Redshift Relation (C3R2) Survey (Masters et al. 2017), the Subaru FOCAS observations of Trump et al. (2011), the Keck MOSFIRE spectra of Trakhtenbrot et al. (2016), the SCUBA-2 spectroscopic redshifts of Casey et al. (2013), the Keck DEIMOS spectra of Kartaltepe et al. (2010), Capak et al. (2011), and Mobasher (2016), the SINFONI spectra of Perna et al. (2015), the zCOSMOS Survey (Lilly et al. 2007), the VIMOS Ultra-Deep Survey (Le Fèvre et al. 2015), the HST/WFC3 grism spectra of Krogager et al. (2014), and the Spitzer/InfraRed Spectrograph spectra of Fu et al. (2010). Our sample includes 20,959 galaxies with spectroscopic redshifts, a spectroscopic redshift fraction of $\sim$17%. If a target is observed by more than one program listed above, we select the spectroscopic redshift from the COSMOS catalog with the highest quality flag. These flags identify the quality of a spectroscopic redshift on the basis of the quality of the original observation, e.g., spectrograph resolution and the number of lines identified during redshift measurement.

2.3. Far-UV–Mid-IR Photometry

To accurately model the emission from ongoing and unobscured star formation, we include point-spread function (PSF)-fit photometric magnitudes from the FUV and near-UV (NUV) bands of the Galaxy Evolution Explorer (GALEX;

Martin et al. 2005), observed down to a limiting magnitude of $m_{AB} \sim 26$. For details on the original data-reduction and PSF-fitting procedures, see Zamojski et al. (2007).

We also include Canada–France–Hawaii Telescope (CFHT) MegaPrime (Aune et al. 2003; Boulade et al. 2003) u^* observations. CFHT u-band observations reach a depth of $m_{AB} \sim 26.4$ with a seeing of $0\rlap{.}''9$ (Capak et al. 2007).

Across the optical continuum, we include Subaru/Suprime-Cam observations from five broad filters (B, V, R, $i+$, $z++$) and 11 medium filters (IA427, IA464, IA484, IA505, IA527, IA574, IA624, IA679, IA738, IA767, and IA827), with a 3σ depth of at least $m_{AB} \sim 25.2$. The maximum PSF FWHM of this filter selection is $1\rlap{.}''89$ (Taniguchi et al. 2007, 2015).

For the near-IR (NIR) emission sampling the old stellar population, we use Vista/VIRCAM (Sutherland et al. 2015) J-, H-, and K-band observations from the UltraVISTA DR-2 survey (McCracken et al. 2012). The UltraVISTA survey observed the J, H, and K bands down to $m_{AB} = 24.7$, 24.3, and 24.0, respectively.

NIR to MIR observations of the COSMOS field were taken by the SPLASH (Steinhardt et al. 2014) and S-COSMOS surveys (Sanders et al. 2007) using the Spitzer Space Telescope (hereafter, Spitzer; Werner et al. 2004).

We include photometry from Spitzer's IRAC's 3.6, 4.5, 5.7, and 7.9 μm bands (for more information, see Fazio et al. 2004), which have PSF widths of $1\rlap{.}''6$, $1\rlap{.}''6$, $1\rlap{.}''8$, and $1\rlap{.}''9$, respectively, and are sensitive down to a 3σ depth of m_{AB} of 25.5, 25.5, 23.0, and 22.9, respectively. To bridge the NIR to the FIR and constrain the MIR continuum and polycyclic aromatic hydrocarbon features, we include 24 μm emission observations that were observed down to a 5σ depth of 71 μJy.

2.4. Herschel Observations

The most important wavelength regime in the estimation of star formation in the gas-rich early universe is the FIR, which helps provide an estimate of the obscured star-forming components of a galaxy. The COSMOS field was imaged using the Herschel Space Observatory (hereafter, Herschel; Pilbratt et al. 2010) Photoconductor Array Camera and Spectrometer (PACS; Poglitsch et al. 2010) 100 and 160 μm bands and the Spectral and Photometric Imaging Receiver (SPIRE; Griffin et al. 2010) using its 250, 350, and 500 μm bands. These observations were performed as part of the PACS Evolutionary Probe (PEP; Lutz et al. 2011) that observed down to a 3σ depth of 5 and 10.2 mJy for the 100 and 160 μm bands, respectively. In addition to PEP, COSMOS was observed as part of the Herschel Multi-tiered Extragalactic Survey (HerMES; Oliver et al. 2012) using SPIRE 250, 350, and 500 μm bands down to a 3σ depth of 8.1, 10.7, and 15.4 mJy, respectively.

Unlike the resolved observations in the optical, the FIR observations from Herschel are subject to blending due to the wide beamwidth ($18\rlap{.}''1$ at 250 μm, $24\rlap{.}''9$ at 350 μm, $36\rlap{.}''6$ at 500 μm). Lee et al. (2010) deblended the sources observed in PEP and HerMES in order of ascending filter FWHM, beginning with Spitzer IRAC observations as priors. Blending is most intense in the SPIRE FIR bands, as they have the widest FWHM of our photometric data set. We deselect FIR photometry from blended targets using the Elbaz et al. (2011) clean index to ensure that only confidently deblended measurements are included. These criteria require no neighbors of comparable ($S_{\mathrm{Neighbor}}/S_{\mathrm{Target}} > 0.5$) flux within $1.1\times$ the

FWHM in 100, 160, 250, 350, and 500 μm. For the Herschel 250 and 350 μm bands, 9095 and 4589 members, respectively, of our initial mass-selected sample have confident nonblended detections. Only 1796 targets have nonblended 500 μm photometry and our results regarding the star formation behavior of the overall sample are consistent within errors when the deblended 500 μm observations are included or excluded in the SED-fitting process.

FIR sources from all bands represent 10% of our total sample, spread roughly homogeneously from $0.3 < z < 2.0$, with $\sim$300 sources per 0.1 Δz increment. This density declines from $z \sim 2$ to $\sim$70 per 0.1 Δz increment by $z \sim 3$. The decline results in the global median SFR becoming more dominated by the rest-frame UV and blue optical emission of the sample at high redshift. Our median SFR results for the bins, discussed in Section 4.2, remain consistent within errors on the median if these FIR detections are excluded. We also find that FIR sources occupy equal density per local environment bin in the high- and low-density bins (described in Section 3.4) used later in our analysis. Therefore, we do not observe a bias toward dense or field environments due to the inclusion of the FIR-detected sources.

3. Methods

3.1. Spectral Energy Distribution Fitting

We estimate the stellar properties of our sample using two SED-fitting packages, MAGPHYS (da Cunha et al. 2008) for the general population and SED3FIT (Berta et al. 2013) for strong AGNs. These packages were chosen due to their capability to manage energy balance and their previous successful use with COSMOS2015 data (Cooke et al. 2019). MAGPHYS uses photometric measurements and errors from $0.0912 \, \mu\mathrm{m} \lesssim \lambda \lesssim 1000 \, \mu\mathrm{m}$ and redshift as inputs. The package fits the data to a library of 50,000 stellar population models (Bruzual & Charlot 2003) and 50,000 dust models (da Cunha et al. 2008) in an energy-balanced manner. MAGPHYS considers the energy radiated from the final stellar model that has been absorbed by the dusty component of the target galaxy and uses this as a prior during the IR fitting (8–1000 μm), ensuring energy balance between the two components. The library models are calculated using an exponentially declining parameterization to model the star formation history, with starbursts included as constant star-forming episodes (da Cunha et al. 2008). For a discussion on the differences between fitting code estimated parameters given a sample population, please see Pacifici et al. (2022). Metallicity models are uniformly included from 0.02 to 2 times the solar value. This method produces a marginalized likelihood distribution of each physical parameter (e.g., SFR, stellar mass) by comparing the total FUV–FIR SED with the distribution of models and corresponding solutions in the template library. Additional details on the computation of the model library can be found in da Cunha et al. (2008). Each target is fit once using this process, yielding SFR and stellar mass estimates with median errors of 13% and 19% the estimated value, respectively.

As the public version of MAGPHYS does not include an AGN component, we use the AGN-capable SED3FIT (Figure 2) to supplement the results produced by MAGPHYS. SED3FIT is a descendant of the MAGPHYS package, using the same stellar and dust models but independently changed to include an AGN library. This is necessary for dominant AGN cases, where the
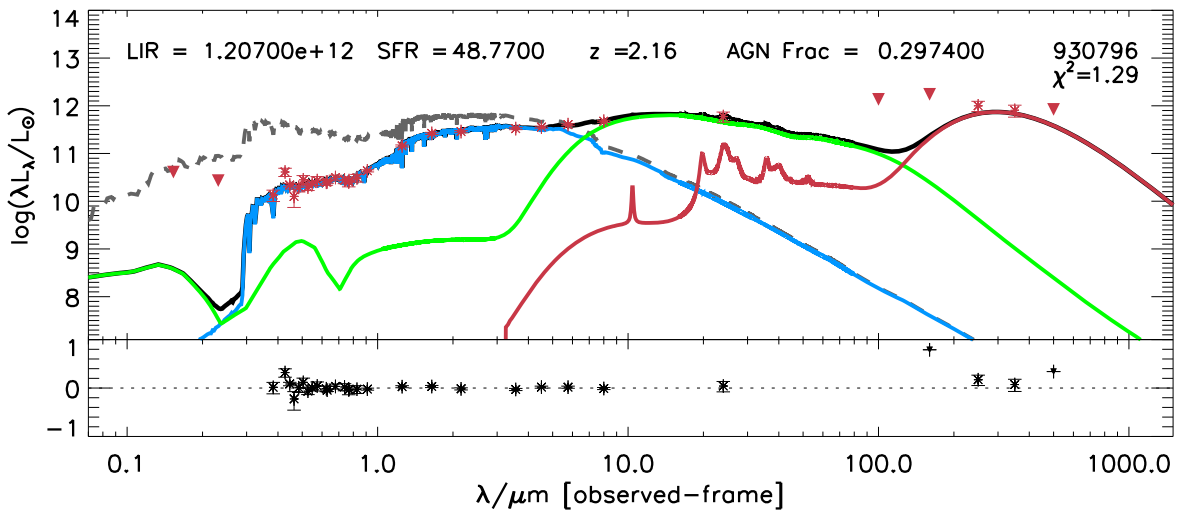
Figure 2. Example SED from a target requiring the use of SED3FIT to fit its MIR emission. The best-ft total model (black) is plotted with the unobscured stellar model (dashed gray), obscured stellar model (blue), AGN torus emission (green), and dust model (red). Photometry used in the fit are plotted as red asterisks, with red triangles used in the case of upper limits in that band. The lower plot shows the fractional residuals between the best-fit total model and the input photometry.

strong UV and/or IR emission from the accretion disk and obscuring torus can cause overestimation of SFRs. From our original mass-selected sample described in Section 2, we identify AGN candidates for refitting with SED3FIT using the 8 μm residuals of the original MAGPHYS fit. If the observed 8 μm emission is greater than 1.4× the modeled 8 μm emission, then the MIR is considered poorly constrained and the source is refit with an AGN component (Cooke et al. 2019; K. D. Tyler et al. 2022, in preparation). This cutoff identifies galaxies with poorly fit IR SED slopes, yielding erroneous SFR and stellar mass estimates. This refitting step is performed rather than fitting the entire sample with SED3FIT because SED3FIT is computationally intensive on large samples and has the inability to determine when an AGN is required at very low AGN fractions. The inclusion of a weak AGN contributing 10% of the bolometric luminosity is easily included in SED3FIT if the fit is degenerate between a weak AGN and no AGN. In the same manner as MAGPHYS, SED3FIT (Berta et al. 2013) first fits a stellar component and uses this fit as a prior to the IR component. However, the difference lies in the simultaneous fitting of an AGN model during these steps using the AGN torus and accretion disk models of Feltre et al. (2012). Energy balance is considered between the stellar and AGN components when fitting the dust emission. For more details on this procedure, and the AGN templates, see K. D. Tyler et al. (2022, in preparation) and Cooke et al. (2019). The number of 8 μm-selected AGN in each redshift bin is included in Table 1, where we find that these 8 μm-selected AGN candidates are a small fraction (<1%) of the overall sample and are predominantly classified as SF galaxies based on their NUVrJ colors (Section 3.2). The median SFR of an AGN fit by SED3FIT is 40% below the estimated MAGPHYS value, and the median AGN stellar mass is 13% lower than the non-AGN MAGPHYS value. However, due to the rarity of AGNs identified using 8 μm residuals in our sample, their inclusion or exclusion in our SFMS estimates do not move our SFMS trends outside their errors.

To test the quality of our fits, we plot a comparison between our final SED-fitting estimates with the original optical–NIR-based estimates from the LePhare results of the COS-MOS2015 catalog (Figure 3). We find strong agreement

between stellar masses derived from LePhare and MAG-PHYS/SED3FIT results, with a median difference below 0.1 dex at $z < 1$ and below 0.2 dex at $z < 3$. Star formation rates are much more variable, especially at higher redshift. Previous papers comparing SED-fitting code results on constant samples have indicated the inclusion of MIR–FIR data points can constrain the obscured SFR component of a SED fit of a SF galaxy (Cooke et al. 2020), lowering the total SFR estimate (Pacifici et al. 2022).

3.2. Color–Color Classification

For reference to the color distribution of our sample, we plot in Figure 4 each galaxy as quiescent or SF using rest-frame k-corrected NUV-r and r-J colors in the COSMOS2015 catalog (Laigle et al. 2016), but do not apply the sSFR cut used in our SFMS estimation. We chose these color criteria to be sensitive to the immediate shutdown of star formation (Ilbert et al. 2013). By using a NUV-sensitive color classification, we probe the distinction between galaxies hosting O- and B-type stars, and those dominated by lower mass stellar types. The result is that galaxy colors transition to the quiescent parameter space faster than purely optical classification methods (Davidzon et al. 2017), which may classify galaxies dominated by A-type stellar emission as SF even when the star formation episode has stopped and the most massive stars born during the latest episode have already died.

We note that we find a low fraction of quiescent galaxies at $z \sim 2$ (~20%–35%) across our entire mass range when using a combined sSFR and NUVrJ color–color cut, substantially lower than the 50% found in K-band-selected spectroscopic programs (Kriek et al. 2006, 2009). However, our values are consistent with the the 35% found when classifying quiescence using sSFR (Toft et al. 2009). Our results are most similar to the SED-fitting results of Toft et al. (2007) and the 20% quiescent fraction found in the spectroscopic survey of the $z \sim 2$ cluster Cl J1449+0856 (Gobat et al. 2013). The difference in quiescent fractions at $z > 2$ between our results and the K-band program is due to the mass selection inherent in the K-band brightness selection used in Kriek et al. (2006), which preferentially selected only galaxies more massive than 10^{11} $M_\odot$. If we select only galaxies from our sample with

Table 1
Star-forming and Quiescent Selected Samples

z	$\log_{10}(M^*_{\mathrm{Limit}})$	Total	SF	Quiescent	Total 8 μm-bright AGNs	SF 8 μm-bright AGNs	Quiescent 8 μm-bright AGNs
0.0–0.3	8.3	5925	4881 (82.4%)	1044 (17.6%)	12	5 (41.6%)	7 (58.3%)
0.3–0.6	8.8	17827	14087 (79.0%)	3740 (21.0%)	33	28 (84.8%)	5 (15.2%)
0.6–0.9	9.2	24079	18122 (75.2%)	5957 (24.8%)	106	75 (70.7%)	31 (29.3%)
0.9–1.3	9.4	27805	21310 (76.6%)	6495 (23.4%)	103	79 (76.7%)	24 (23.3%)
1.3–1.7	9.8	15131	10483 (69.3%)	4648 (30.7%)	57	33 (57.9%)	24 (42.1%)
1.7–2.2	10.0	11055	8298 (75.1%)	2757 (24.9%)	89	63 (70.8%)	26 (29.2%)
2.2–2.7	10.1	5215	3261 (62.5%)	1954 (37.5%)	63	48 (76.2%)	15 (23.8%)
2.7–3.5	10.2	4500	3102 (68.9%)	1398 (31.1%)	23	17 (73.9%)	6 (26.1%)

Note. Galaxies selected from the COSMOS2015 catalog above the stellar mass completion limit. We identify star-forming (SF) and quiescent galaxies using NUVrJ rest-frame colors (Ilbert et al. 2013) and a specific star formation rate (sSFR) cut of $10^{-11}(1+z)^{2.5}$ yr^{-1} (Ilbert et al. 2010; Domínguez Sánchez et al. 2011), and identify 8 μm-bright AGN candidates using 8 μm fitting residuals from MAGPHYS. These AGNs do not represent all AGN types in our sample, only the IR-bright sources which require an AGN component to accurately estimate SFRs from their IR luminosity. We chose a NUVrJ selection criteria to be sensitive to <billion year timescale star-forming episodes (Arnouts et al. 2007; Salim et al. 2007). We do not find a significant difference in the distribution of quiescent and SF galaxies between the MAGPHYS and SED3FIT samples. Note that the star-forming and quiescent fractions are computed over our entire stellar mass range at that redshift. The difference between star-forming and quiescent fractions here and the distribution shown in Figure 4 is due to the sSFR cut used in this table, which identifies some blue galaxies as quiescent due to their low sSFR ($<10^{-11}(1+z)^{2.5}$ yr^{-1}). These may represent a subpopulation of galaxies which have just shut down their star formation.

stellar masses greater than 10^{11} $M_\odot$, we rederive the 40%–50% quiescence fraction seen in Kriek et al. (2006).

3.3. Characterizing Morphology

To determine whether the flattening of the SFMS can be explained by the growth of the bulge component of SF galaxies, we require morphological decomposition measurements across a wide range of area and redshift. These classifications enable us to select disk- and bulge-dominated systems, and estimate the SFMS relation of each population. If the flattening is purely due to bulge growth, then the disk-dominated systems will exhibit more constant sSFR while the bulge-dominated systems will exhibit a stronger characteristic turnover of SFR above a mass cutoff. Due to the wide range of redshift covered in our analysis, it is essential to use rest-frame optical morphological measurements. This means that it is necessary to use an optical classification catalog at $z < 1$ and a NIR classification for our high-redshift targets. Therefore we perform the same analyses using two different COSMOS morphological catalogs.

At low redshift ($z < 1$), we retrieve optical classifications from the Zurich Structure & Morphology Catalog (Sargent et al. 2007; Scarlata et al. 2007). This catalog uses principal component analysis of five nonparametric diagnostics: asymmetry, concentration, Gini coefficient, second-order moment of the brightest 20% of galaxy pixels (M20), and ellipticity. In addition, these diagnostics are used in tandem with single Sèrsic fits of the surface brightness distribution to determine a bulgeness parameter correlated with the bulge-to-disk ratio. This is the value from the catalog used to identify disk-dominated galaxies among the full set of disk galaxies, referred to as Type-2 galaxies in the catalog. The Zurich catalog includes ∼130,000 targets across the full 2 square degrees of the COSMOS HST/Advanced Camera for Surveys (ACS) F814W mosaic down to a limiting magnitude of $I_{AB} \sim 24$. We select Type-2 galaxies with a bulgeness parameter of 2 or 3 (disk-dominated composites and purely disk dominated, respectively) for our disk-dominated sample. Bulge-dominated Type-2 galaxies are identified with a bulgeness parameter of 0 or 1. For full details on this classification system, see Sargent et al. (2007) and Scarlata et al. (2007). Scarlata et al. (2007)

verified the quality of these fits by visually inspecting the results and removing spurious cases such as overblending and false detections. The median reduced χ^2 of the fits for the targets in both our sample and the full Zurich catalog is 1.04.

At higher redshift ($z > 1$), we estimate rest-frame optical morphological parameters using the IR HST/WFC3 observations of the COSMOS field taken as part of the Cosmic Assembly Near-IR Deep Extragalactic Legacy Survey (CANDELS) treasury program (Grogin et al. 2011; Koekemoer et al. 2011) supplemented by the publicly available WFC3/IR imaging available through the Mikulski Archive for Space Telescopes (MAST). We choose to limit our high-z morphology sample to galaxies observed with the F125W, F140, or F160W filters, probing the rest-frame optical ($\lambda_{observed} > 600$ nm) for galaxies at $z > 1$. These filter selections, in combination with the partial area of the COSMOS field observed with these filters, produces a sample of 4252 galaxies, roughly 5% of the $z > 1$ sample.

To characterize the morphology of as many galaxies at high redshift ($z > 1$) as possible, we use the MAST Portal to retrieve all public WFC3/IR F125W, F140W, and F160W science observations from the COSMOS field that have not already been used as input to GALAPAGOS-2 during the initial CANDELS-COSMOS program (Table 2). We also do not include data from COSMOS-DASH due to the low surface brightness achieved per WFC3 observation (Mowla et al. 2019). In the case of multiple programs over the same object we use an exposure from the longest exposure program at that location. We also include the HST/ACS F814W images available from the COSMOS field ACS mosaic (Koekemoer et al. 2007) in our high-redshift morphology fitting. We use the same pipeline as the original GALAPAGOS-2 CANDELS-COSMOS morphological classification, ensuring we can fairly combine the derived morphological measurements. Examples of each morphology bin are included in Figure 5.

The high-redshift fitting was performed using packages from the project MegaMorph (Häußler et al. 2013), which developed a modified version of the GALAPAGOS IDL code (Barden et al. 2012) that takes advantage of a multiwavelength version of the Galfit fitting routine (Peng et al. 2002, 2010). This multiband fitting package is titled GALAPAGOS-2 (Häußler
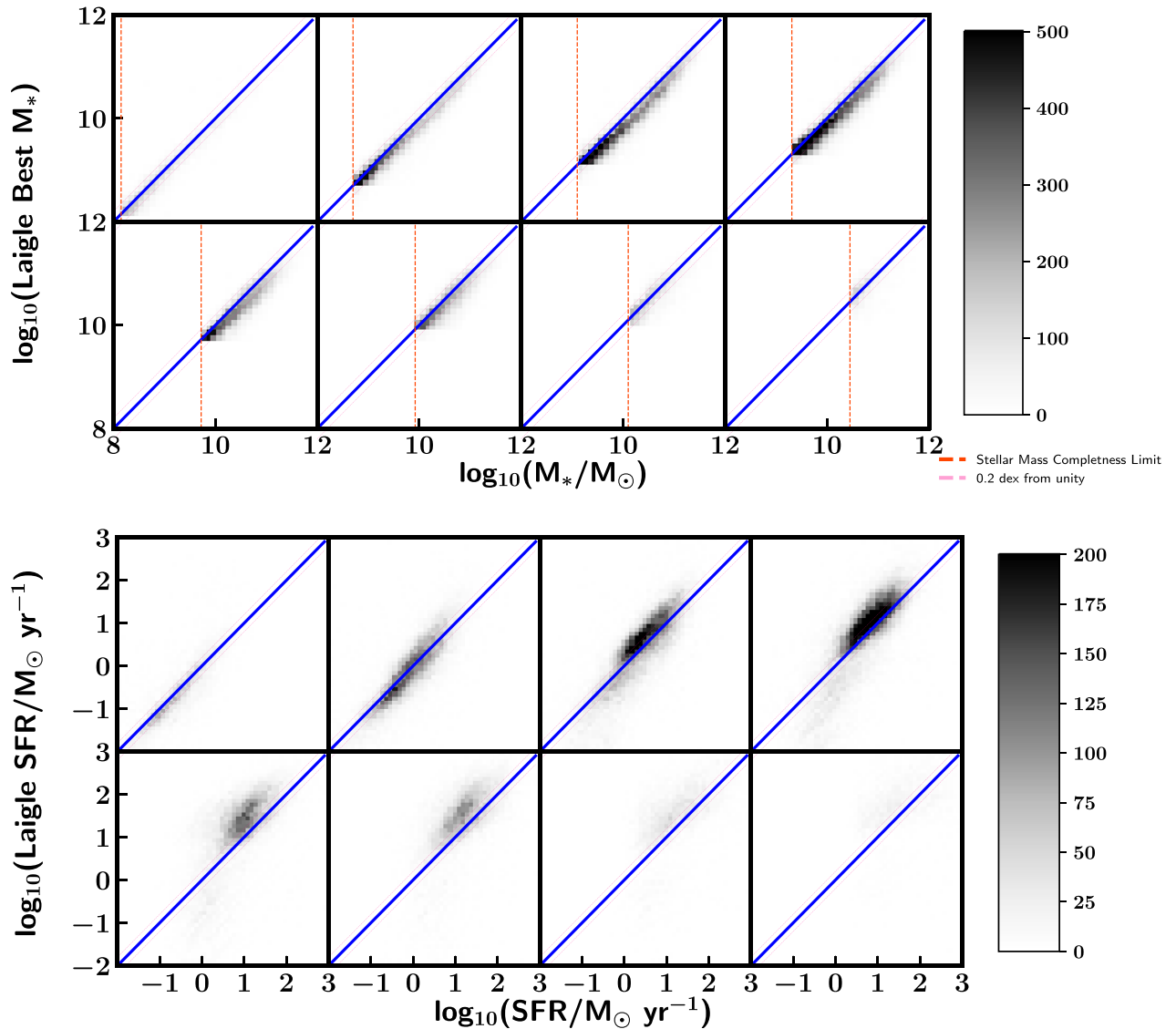
Figure 3. Top: the stellar mass distribution of our refit sample in comparison to the original optical–NIR-based fitting results of Laigle et al. (2016). We find strong agreement within the two samples, with a dispersion on par with 0.2 dex. This is consistent with previous comparisons between SED-fitting codes (Pacifici et al. 2022). Bottom: the same Laigle and MAGPHYS-SED3FIT result comparison using total estimated SFR. We find significantly more scatter, which was an expected result due to our inclusion of MIR–FIR data. The use of MIR–FIR data in SED fits constrains an other otherwise unconstrained obscured star-forming component, yielding lower SFRs when included (e.g., Cooke et al. 2020).

et al. 2022), and provides wavelength-dependent, two-component Sèrsic fit parameters for bulge–disk decomposition. We input into GALAPAGOS-2 postage stamps of any sample member observed by both the HST/ACS F814W COSMOS full-field mosaic and any combination of public HST/WFC3 F125W, F140W, and/or F160W observations. The output provides best-fit parameters for each Sérsic component. Specifically, we use the magnitude of each component to estimate bulge-to-total (B/T) luminosity ratios of each galaxy run through the pipeline. GALAPAGOS-2 provides these parameters for each filter an object was observed in, ensuring we can consistently use parameters derived from rest-frame optical continuum emission across our sample. While GALAPAGOS-2 is capable of interpolating between filters, we recognize the difficulty of doing so with so few filters and use the best-fit solution from a target's longest wavelength observation to best estimate the distribution of the stellar population. We find that the B/T ratio from targets with combinations of F125W, F140W, and

F160W display consistent B/T ratio solutions when using the magnitudes from each filter. Shorter wavelength filters such as F110W and F105W were tested but did not consistently reproduce results from longer wavelength observations and were therefore not included in this work.

GALAPAGOS-2 has already been used in two-component mode on the HST/WFC3 images from all five CANDELS fields (Grogin et al. 2011; Koekemoer et al. 2011), and for each filter any given object has been observed. We include these values in addition to the estimates made in this work. We note that substructure at high redshift can make the estimation of morphology difficult.

These targets exhibit a median reduced $\chi^2 \sim 0.25$, a value potentially indicating the presence of overfitting due to the high number of free parameters involved in the two-component Sérsic fit needed to identify disk-dominated systems. The magnitudes of each component are well defined, with a median magnitude error ~ 0.1 mag. Therefore, we make the caveat that
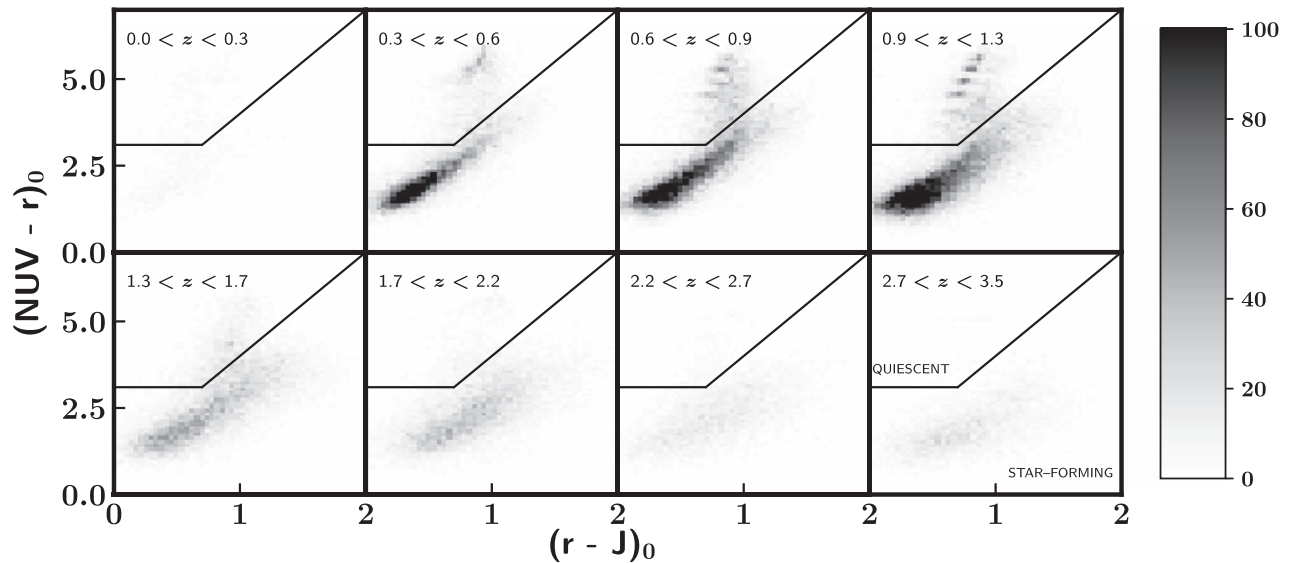
Figure 4. The distribution of star-forming and quiescent galaxies in our sample as defined by rest-frame NUV-r and r-J colors (Ilbert et al. 2013). We find that the fraction of quiescent galaxies increases by roughly an order of magnitude over our redshift range. We include the fractions of galaxies in each subsample in Table 1.

the following results from this analysis are most applicable across the population rather than for specific targets. Additionally, any complex gas and star-forming structures of high-z SF galaxies would contribute to a more distributed surface brightness distribution, which remains our measure for disk-dominated systems. While the exact structure of the disk may be different at high z, the investigation of the distributed star-forming component of high-z galaxies remains our focus and remains roughly identifiable given our data; see Hashemizadeh et al. (2021) for a discussion on visually identified substructure with increasing redshift and the need for a two-component bulge and disk morphological model.

While we caution that these two catalogs both measure morphology, they do so in very different ways and should not be used together. Therefore, we perform any morphological analysis of our sample with each morphological catalog treated independently in Section 5.3, and examples of the classification with images from each data set are available in Figure. 5. To verify that they produce similar enough results for the sake of discussion, however, we compare the Zurich single Sèrsic profile index with the overall index of the two-component Sèrsic profile fits from GALAPAGOS and find that, for a given target in both catalogs, the median single component Sèrsic index is 12% lower than the median composite Sèrsic index of the GALAPAGOS result.

3.4. Quantifying Local Environment

Finally, we require a local environment measurement to determine whether SF galaxies reside in a given spatially dense region at their redshift, and we can use that measurement to identify any environment-dependent behavior. We quantify the local environment for each galaxy using the weighted adaptive kernel smoothed maps of the COSMOS field (Darvish et al. 2015). The spatial density field is calculated in overlapping redshift slices. Each galaxy within a slice is assigned a weight proportional to the likelihood of the redshift estimate lying within the slice. This likelihood is the fraction of the galaxy's photo-z probability distribution function (PDF) that lies within the redshift slice. With these weights as a prior, Darvish et al. (2015) smoothed the spatial density field using a Gaussian

kernel with a "global" width of 0.5 Mpc. For reference, this size corresponds to the typical virial radius of X-ray groups in the COSMOS field (Finoguenov et al. 2007; George et al. 2011). Therefore, these maps should be considered most accurate for identifying the cores of clusters and large galaxy groups. With the parameters used in this specific data set, filaments will be less likely to be detected, as this smoothing width is similar to prior widths frequently applied when identifying filaments from density maps (e.g., Tempel et al. 2014). The density maps provide density values at each location as a multiple of the median density of the map at that given redshift slice. For further details on this method, see Darvish et al. (2015).

We consider galaxies in three environment bins: those residing in regions below the median density ($\delta < \delta_{Median}$, field regions), between median density and twice the median density ($\delta_{Median} < \delta < 2\delta_{Median}$, intergroup regions), and regions with any density greater than twice the median density ($\delta > 2\delta_{Median}$, dense regions). Dense environments are confidently recoverable in the maps below $z \sim 2.5$, where photo-z errors are ~ 0.01 (Darvish et al. 2014). Maps at $z > 2.5$ recover large-scale features, with photo-z errors of the order ~ 0.10 (tens of Mpc), however the intergroup classification will not reliably detect filamentary structures. To verify that the smoothed maps were sufficiently wide in comparison to our sample's photo-z errors, we calculated the median photo-z for each slice's subsample. We show in Figure 6 that the median photo-z error of our mass-selected sample is similar to the width of each map slice until $z > 2.2$. Above this redshift the maps contain the peak, but no longer the majority, of the median photo-z PDF.

4. Results

4.1. The Shape of the Star Formation Main Sequence

After we fit the SEDs of all galaxies selected in Section 2.1, we recalculate the stellar mass completeness. Due to the possibility of stellar mass estimates scattering below the original stellar mass cutoff, we redefine our stellar mass selection to include galaxies with stellar mass above the Laigle completeness limit plus the median stellar mass error for that

Table 2
WFC3/IR Input to GALAPAGOS-2

WFC3/IR Filter	Program ID	PI
F125W	12461	Riess, Adam
F125W	13046	Kirshner, Robert P.
F125W	13294	Karim, Alexander
F125W	13384	Riechers, Dominik A.
F125W	13641	Capak, Peter Lawrence
F125W	14750	Wang, Tao
F125W	14895	Bouwens, Rychard
F125W	15115	Silverman, John David
F125W	15910	Daddi, Emanuele
F140W	12190	Koekemoer, Anton M.
F140W	13792	Bouwens, Rychard
F140W	13793	Bowler, Rebecca A. A.
F140W	14495	Sobral, David
F140W	14719	Best, Philip N.
F140W	14808	Suzuki, Nao
F140W	15115	Silverman, John David
F140W	15363	Suzuki, Nao
F140W	15862	Finkelstein, Steven L.
F160W	12167	Franx, Marijn
F160W	12440	Faber, Sandra M.
F160W	12461	Riess, Adam
F160W	12578	Forster Schreiber, N. M.
F160W	12990	Muzzin, Adam
F160W	13046	Kirshner, Robert P.
F160W	13294	Karim, Alexander
F160W	13384	Riechers, Dominik A.
F160W	13641	Capak, Peter Lawrence
F160W	13657	Kartaltepe, Jeyhan
F160W	13868	Kocevski, Dale D.
F160W	14596	Fan, Xiaohui
F160W	14699	Sobral, David
F160W	14721	Conselice, Christopher J.
F160W	14750	Wang, Tao
F160W	14895	Bouwens, Rychard
F160W	15229	Daddi, Emanuele
F160W	15692	Faisst, Andreas L.
F160W	15910	Daddi, Emanuele

Note. The programs used as input for GALAPAGOS-2. Exposures were retrieved using a radial search of 1°.2 from the COSMOS field center. For ease of the reader we list the unique program IDs and PIs.

redshift bin. This removes the parameter space where SED estimate scatter may remove targets and compromise completeness. The effect of this choice raises the stellar mass limit from Laigle et al. (2016) by 0.1 dex from $0.0 < z < 1.3$ and 0.2 dex between $1.3 < z < 2.2$.

To estimate the form of the SFMS, we select the star-forming population using NUVrJ color–color criteria (Ilbert et al. 2013) and a redshift-dependent sSFR cut corresponding to $>10^{-11}$ yr^{-1} at the present day (Ilbert et al. 2010; Domínguez Sánchez et al. 2011). NUV, r-, and J-band magnitudes are taken from the k-corrected rest-frame absolute magnitudes provided in COSMOS2015. The sSFR cut evolves with redshift according to a factor of $(1+z)^{2.5}$, motivated by the results from nonstacked samples of Speagle et al. (2014). We consider this a less restrictive choice, as observed values for $(1+z)^{\gamma}$ may vary from $\gamma = 2$–5 (Salim et al. 2007; Karim et al. 2011; Whitaker et al. 2014; Pearson et al. 2018; Popesso et al. 2019) and overestimation of γ may yield samples biased toward the starbursting side of the SFMS. We include a second cut based

on NUVrJ colors to remove potentially rejuvenated quiescent galaxies. Several mechanisms exist to replenish the cold gas supply of formerly quiescent galaxies, such as the accretion of H I gas from their local environment or the accretion of a gas-rich merger companion (e.g., Kaviraj et al. 2009). We identify 2258 objects (1.8% of our total sample) in our original sSFR-selected star-forming sample with red colors which could be these rejuvenated interlopers that are star-forming yet not undergoing the traditional track of SF galaxies along the SFMS. For further discussion on our color selection, see Section 3.2.

We fit the SFRs and stellar masses of our star-forming sample with a broken power law using the functional form of Lee et al. (2015),

$$\log_{10}(SFR) = S_0 - \log_{10}\left[1 + \left(\frac{M}{M_0}\right)^{-\gamma}\right], \quad (1)$$

where S_0 represents the highest estimated SFR in the sample, M_0 is the turnover mass for the broken power law, and γ is the power-law slope at low stellar masses. All three parameters are left free during the fitting process to not bias our results toward fits with a turnover or those without. A lack of a turnover is identified if the turnover mass is greater than the maximum stellar mass of our sample. The evolution of higher turnover mass with look-back time has been observed in previous works (e.g., Thorne et al. 2021). We weight each galaxy by the inverse of the reduced χ^2 of the best-fit SED. Our sample is well fit with a peak of the reduced χ^2 distribution $\sim$1 and an evolving median value of $\sim$1.5–2.0 with increasing redshift. Confident in the overall quality of our fit sample, this weighting practice minimizes the effect of outliers that may have extremely high SFR estimates or poorly defined SFR estimate PDFs. Our best-fit parameters are listed in Table 3. We find that the turnover mass (M_0) evolves toward higher stellar masses from the present day to $z = 1.3$. At $z > 1.3$, the turnover mass is best fit by a value greater than the masses in the sample. This form is effectively linear, a trend also found in Leslie et al. (2020) and Tomczak et al. (2016).

The distribution of our sample's SFR and stellar mass estimates in eight redshift bins from $0 < z < 3.5$ are shown in Figure 7, using the same redshift bin definitions as Laigle et al. (2016) with our best-fit SFMS function overplotted in comparison to relevant counterparts in the literature. As observed in previous SFMS studies out to $z \sim 2.5$ (Whitaker et al. 2012, 2014; Lee et al. 2015), the normalization of the SFMS increases with increasing redshift, i.e., galaxies at a fixed stellar mass have higher SFRs at higher redshift. We also find a turnover of SFR with stellar mass above $10^{10} M_{\odot}$ for $z < 1.3$, where galaxies of progressively higher stellar mass no longer exhibit higher SFRs. The turnover mass also evolves to higher stellar mass with increasing redshift. The high-mass turnover has been previously observed in the literature (e.g., Whitaker et al. 2014; Schreiber et al. 2015), and specifically in the COSMOS field (Lee et al. 2015; Leslie et al. 2020; Thorne et al. 2021).

The slope of the global SFMS is a measurement with significant scatter in the literature, with slopes ranging between 0.5 and 1, the same range exhibited by our sample in Figure 8. This high variation is present regardless of whether the parent sample was chosen via UV, optical, or IR characteristics
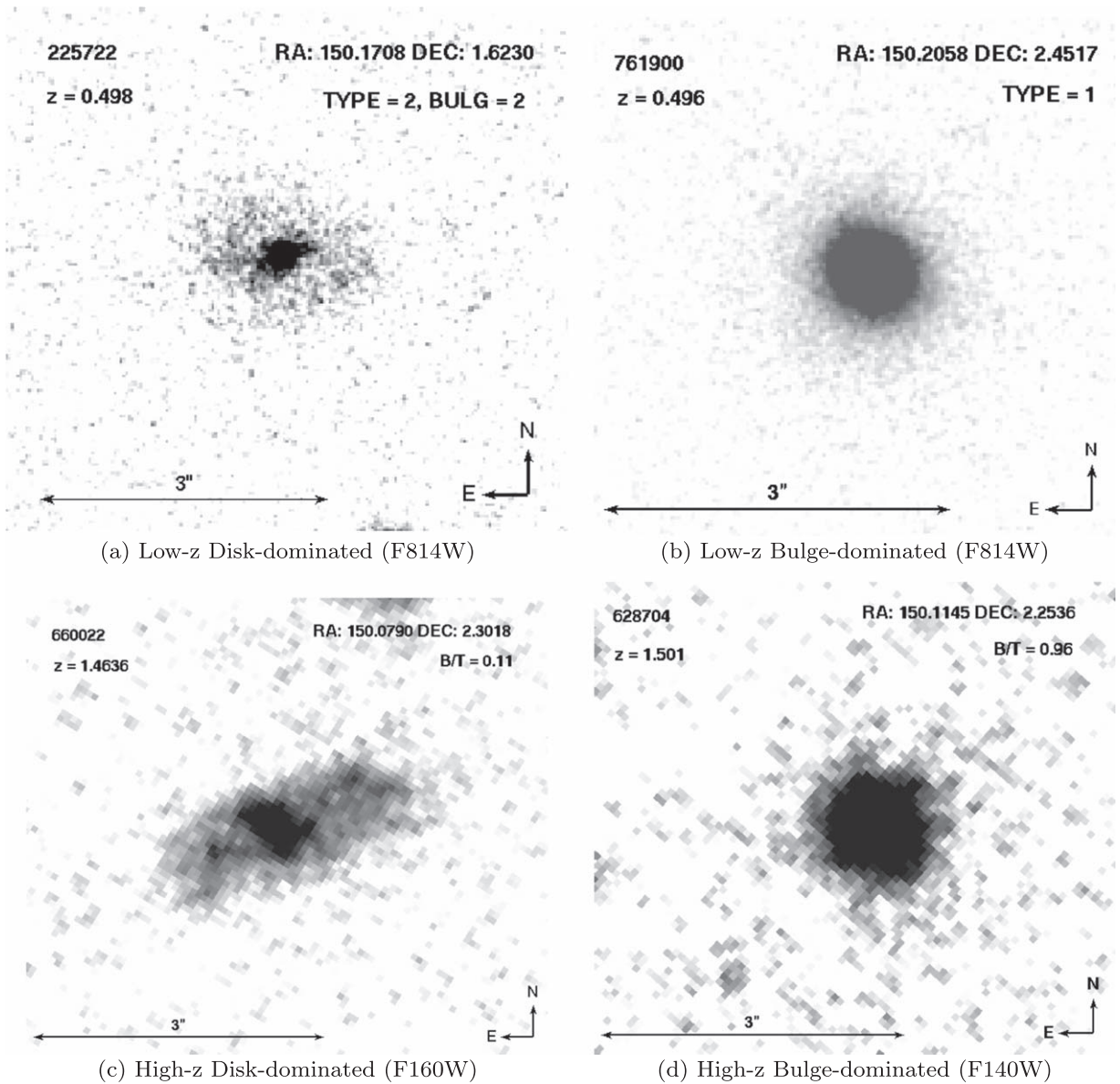
(a) Low-z Disk-dominated (F814W)

(b) Low-z Bulge-dominated (F814W)

(c) High-z Disk-dominated (F160W)

(d) High-z Bulge-dominated (F140W)

Figure 5. Examples of disk- and bulge-dominated galaxies from both redshift samples. The low-z sample images are taken from the COSMOS field HST ACS/F814W mosaic with morphological-type labels from the Zurich morphological catalog. The high-z sample uses images taken using HST/WFC3 F140W and F160W for these examples and a bulge-to-total ratio calculated using the GALAPAGOS-2 package.

(Speagle et al. 2014). In Figure 8, we plot the slopes of the SFMS for high- and low-mass bins using both our own turnover mass estimate and the $10^{10}\,M_*$ value commonly used throughout the literature. Using the literature turnover, we find a convergence in the high- and low-mass slopes at $z > 1$. Using our turnover estimates, we find that the high-mass end of the SFMS flattens out to $z > 1$. At high redshift, the low-mass end is too loosely constrained to make any conclusions, while the high-mass end rises in slope toward linearity. We tested using an evolving mass cut motivated by our SFMS fits and found that the high-mass bin at $z > 1$ is often too poorly constrained to make any conclusions.

4.2. Estimating the Star Formation–Stellar Mass Relation in Different Environments

We compare the SFMS across three environment bins without consideration of morphology in order to probe the local

environment's role on the quenching of SF galaxies as exhibited by the shape and normalization of the SFMS. In Figure 9, we compare the behavior of our fit to the global SFMS to the median SFR per stellar mass bin in field ($\delta < \delta_{\mathrm{Median}}$, blue), intergroup ($\delta_{\mathrm{Median}} < \delta < 2 \times \delta_{\mathrm{Median}}$, green), and dense ($\delta > 2 \times \delta_{\mathrm{Median}}$, red) environments. When comparing the shape and position of the SFMS within each environment bin, we find no difference in median sSFR with environment. One difference between our environment-binned sample and the overall sample is an offset in sSFR. This is due to the reduced-χ^2 weighting used in the trend estimation for the total population, which favors higher sSFR galaxies. With either method, we still observe a decline of sSFR with mass across all redshifts and across all environments.

The consistent decline of sSFR with stellar mass across environment bin is also observed when moving across redshift bins. This result leads to the conclusion that SF galaxies are forming stars in a self-similar manner independent of the local
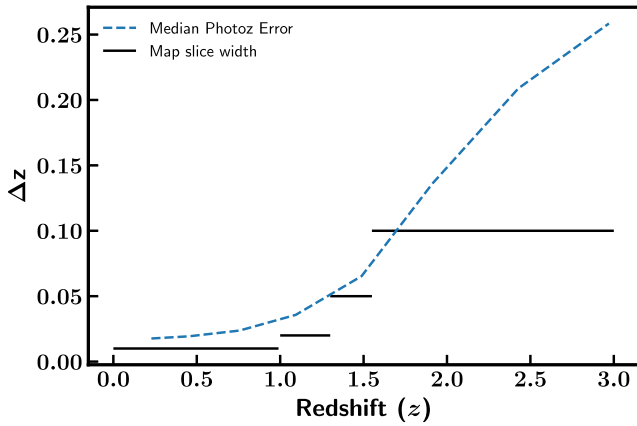
Figure 6. To characterize the strength of the local environment estimates used here, we compare the median photo-z error of our mass-selected sample as a function of redshift with the redshift slice widths of each map. Map widths were originally constructed with increasing widths with redshift. We find that the majority of each target photo-z distributions is well contained by each map slice until $z \sim 2.2$, where the photo-z PDF 68th percentile is twice the width of the environment slice.

Table 3
Star Formation Main Sequence Best-fit Function Parameters

z	S_0	M_0	γ
0.0–0.3	1.00	11.15	0.67
0.3–0.6	1.01	10.68	0.77
0.6–0.9	1.45	11.03	0.71
0.9–1.3	2.05	11.84	0.60
1.3–1.7	10.26	24.51	0.64
1.7–2.2	9.20	21.44	0.72
2.2–2.7	9.34	21.81	0.69
2.7–3.5	3.49	12.70	0.80

Note. Best-fit Lee et al. (2015) broken power-law parameters using Equation (1) and the star-forming sample in each of our redshift bins. S_0 represents the highest estimated SFR in the sample, M_0 is the turnover mass for the broken power law, and γ is the power-law slope at low stellar masses. The rise of M_0 represents a transition from a SFMS with a turnover at low z ($z < 1.3$) to without a turnover at high z ($z > 1.3$).

galaxy density surrounding them, and that star formation's insensitivity to local environment (previously observed at low redshift) is itself insensitive to redshift out to $z \sim 3$.

To further understand this behavior, we use our NUVrJ color criteria and SFR estimates to examine the behavior of both SF and quiescent galaxies in our dense and field environment bins to determine whether the quiescent population shows evidence of environmental dependence and where the quiescent population lies with respect to the star-forming population. By binning each environment bin by star-forming or quiescent status, we can answer whether there is any difference in the quenching behavior and star formation end state, quiescent galaxies, in each environment. In Figure 10 we plot the median sSFR per stellar mass bin of 150 objects for both star-forming and quiescent galaxies across dense and field environments. To test how our combined sSFR and color selection criteria affect the sample, we only use the NUVrJ color criteria to select the star-forming sample of Figure 10, and plot the sSFR delineator of galaxies with sSFR $= 10^{-11}$ yr$^{-1}(1+z)^{2.5}$ as a black line for comparison. We find that at $0.9 < z < 3.5$, both star-forming and quiescent subsamples do not show any difference in median SFR based on local environment. We note that the

median SFR of the purely color-selected SF galaxies observed here approaches the sSFR cutoff at high z ($z > 1.3$), however the median remains above the sSFR cutoff within the errors on the median. Additionally, the shape of the SFMS, as plotted in Figure 10 using stellar-mass-binned medians, does not significantly change with redshift.

4.3. The Role of Morphology in the Star Formation Main Sequence

To address whether the turnover of the SFMS is due to a transition toward bulge-dominated systems, we study the shape of the SFMS for bulge- and disk-dominated SF galaxies. Due to the wide redshift range used here, any morphological catalog would only measure the distribution of stellar populations within a wavelength-dependent range. Therefore, we perform two independent morphological analyses: first, a low-z assessment using observer-frame optical data, and second, a high-z sensitive assessment using observer-frame NIR data.

4.3.1. Low-z Morphology Using Optical Measures

First, in Figure 11, we consider our low-redshift morphological sample using classifications from the Zurich Structure & Morphology Catalog (Sargent et al. 2007; Scarlata et al. 2007). Due to the rest-frame optical wavelengths of this catalog, classifications only accurately probe the bulk of the stellar component out to $z \sim 1$, but are classified across the entire COSMOS field, yielding a uniform data set across the COSMOS field. For disk-dominated late types, we use the classification of TYPE = 2 and BULG = 2 or 3 to only select pure disks and disk-dominated composites. These classifications are derived using principle component analysis and correlated with, but limited by, bulge-to-disk ratios. For further information on this analysis, please see Scarlata et al. (2007). These criteria are consistent with previous COSMOS morphological studies using the Zurich catalog (e.g., Molnár et al. 2018).

Bulge-dominated disk galaxies are selected using galaxies with a disk morphology but the high bulge dominance labels of BULG = 0 or 1. Finally, we also include ellipticals as their own bin using the Zurich morphology TYPE = 1, without any overlap with our bulge-dominated disk subsample. We find that a decline in sSFR with total galaxy mass remains in the disk-dominated sample and is also consistent within the errors on the median trend across all three morphology bins at $z < 1.3$. We consider this as evidence for a declining host sSFR with stellar mass, irrespective of the dominance of the bulge component.

4.3.2. High-z Morphology Using Near-IR Measures

To determine whether any bulge-dependent effect is driving the turnover at high masses at high redshift, we perform a similar analysis using the two-component Sérsic fits available in the CANDELS MegaMorph catalog supplemented with new two-component decompositions performed using an identical pipeline on the publicly available HST WFC3/IR F125W, F140W, and F160W images covering the COSMOS field, as described in Table 2. This second analysis enables us to reach higher redshift than the Zurich catalog due to the longer wavelengths observed with HST WFC3/IR filters. The multi-band approach of the GALAPAGOS-2 pipeline also enables the separation of bulge and disk components more cleanly
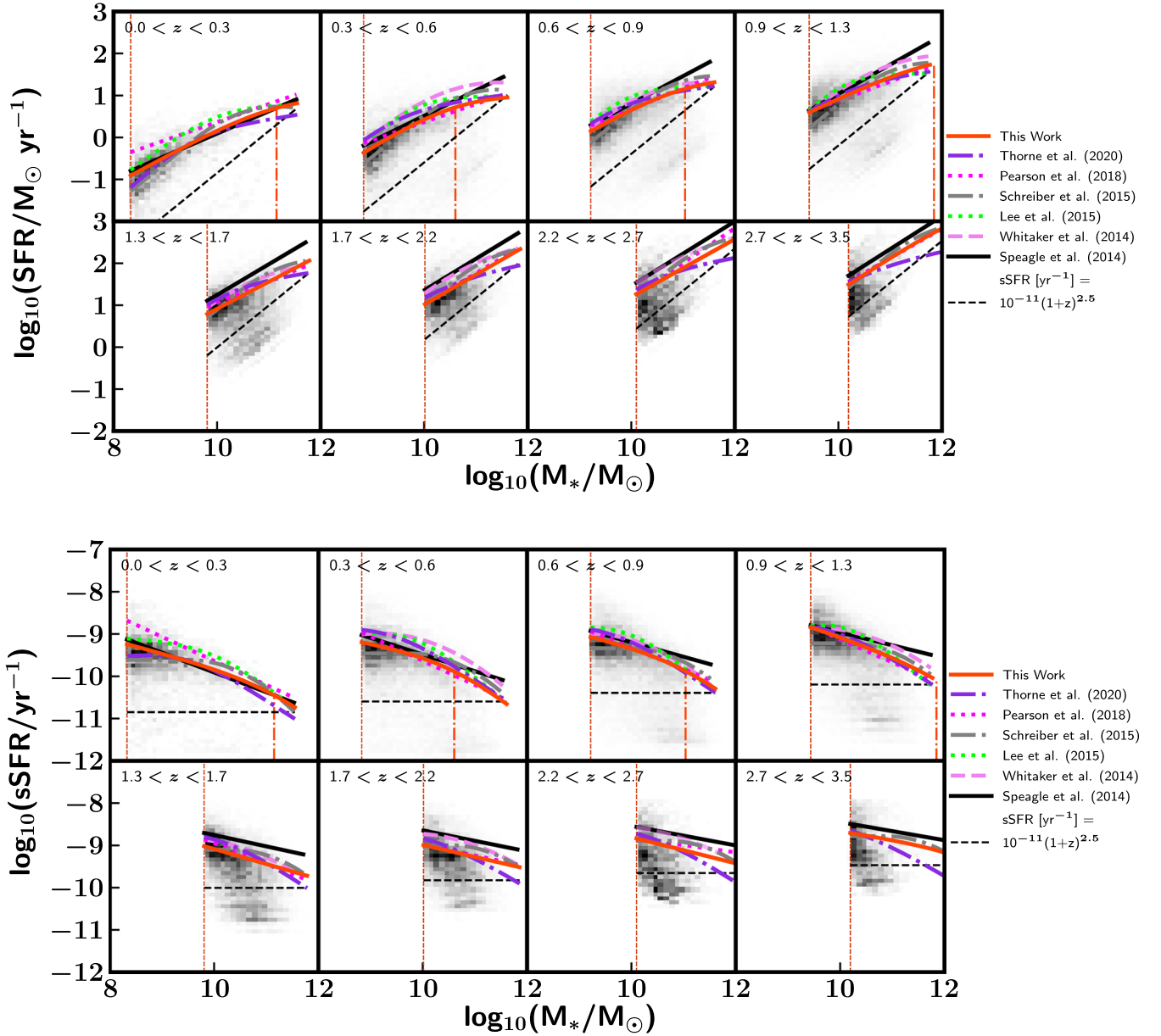
Figure 7. Top: density plot of star formation rate vs. stellar mass in each redshift bin of our total (star-forming+quiescent) sample. For the illustrative use of this plot, we have not normalized the underlying density plot to better show the distribution of low-numbered populations, e.g., our lowest redshift bin. The solid orange-red line corresponds to the broken power-law fit (described in Equation (1)) to the star-forming population in each redshift selected using NUVrJ color–color criteria (Section 3.2) and a specific star formation rate (sSFR) cut of $>10^{-11}(1+z)^{2.5}$ yr^{-1}. The estimated turnover mass is indicated using an orange dashed–dotted line below the SFMS estimate line. The SFMS becomes linear at $z > 1.3$ and has no associated turnover mass. Bottom: we move to a sSFR space for the remainder of the paper to better articulate the evolution of star formation efficiency with stellar mass. For both plots, we plot the SFMS trends observed by Whitaker et al. (2014), measured from $0.5 < z < 2.5$, as a fuchsia dashed line, Speagle et al. (2014) as a solid black line, Thorne et al. (2021) as a violet dashed–dotted line, Lee et al. (2015) as a dotted green line, Pearson et al. (2018) as a dotted fuchsia line, and Schreiber et al. (2015), renormalized to a Chabrier (2003) IMF, as a gray dotted–dashed line. The stellar mass completeness limit for each redshift bin is plotted with a vertical dashed line in orange. The lack of massive, quenched galaxies between $0 < z < 0.6$ is a cosmological effect due to the limited volume of COSMOS at low redshifts (2.26×10^6 Mpc^3 in COSMOS below $z < 0.6$).

(Häußler et al. 2022), enabling analysis to fainter galaxies and greater distances. The model component magnitudes provided by GALAPAGOS-2 can be used to select an explicit B/T ratio cutoff to select disk-dominated, bulge-dominated, and intermediate galaxies.

4.3.3. Results from Low- and High-z Samples

We limit our disk-dominated sample to those with confidently low B/T ratios, defined as a B/T ratio of <0.25. Bulge-dominated galaxies are selected with B/T > 0.75 and

intermediates as 0.25 < B/T < 0.75. This requirement ensures our disk-dominated sample only considers galaxies in which the bulge is not the dominant environment for the stellar population of a given galaxy. Similar cutoffs are used in the literature to form bulge- and disk-dominated samples to compare against each other (e.g., Kennedy et al. 2016). Shown in Figure 12, we find that at $z < 1.3$ the SFMS of disk-dominated systems experiences a weak decline with stellar mass consistent with the turnover exhibited by the overall SF population. We also see that each morphology bin exhibits a decline within each of the B/T classifications within their
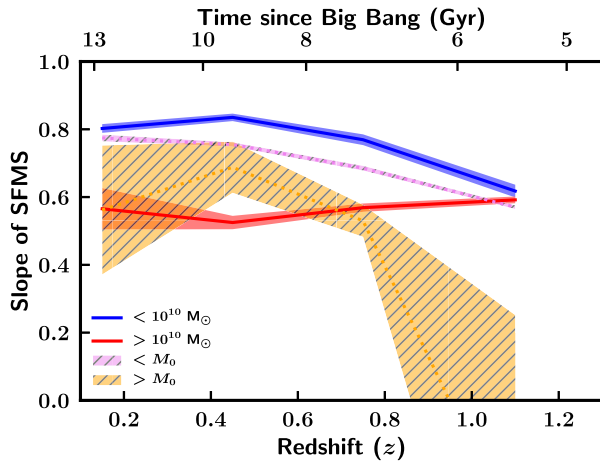
Figure 8. The slope of the star formation–stellar mass relation for all star-forming (SF) galaxies, calculated using a first-order least-squares polynomial fit for galaxies above (red) and below (blue) the literature turnover of the relation (10^{10} $M_{\odot}$), weighted by reduced χ^2. We compare this literature-based measurement of our sample to the slopes when measured using our estimates for the "knee" of the SMFS, M_0 (violet hatched for greater than the knee, violet orange for below the knee). The uncertainties of the fits are plotted as shaded regions. We find that at $z > 1$, the best-fit SFMS M_0 becomes higher than the stellar masses of our sample, indicating a linear relation. We find that the high-mass end decreases in slope strongly with redshift while the low-mass slope only decreases by 30% by $z \sim 1$. In comparison, the fixed SFMS knee of 10^{10} used in the literature will include SF galaxies from 10^{10} to $10^{10.5}$ in their high-mass sample, a mass range that is less sensitive to the decrease in SFR with redshift, decreasing the redshift dependence of the fixed-mass-selected high-mass slope.

errors (B/T < 0.25, 0.25 < B/T < 0.75, and B/T > 0.75). We caution that the results of our $0.9 < z < 1.3$ bin are subject to the F814W filter no longer probing the old stellar population due to the light redshifting out of the rest-frame optical, and therefore targets may have underestimated bulge components in this panel.

In the rarely examined morphology parameter space of $z > 1.3$ plotted in Figure 12, we work with a significantly less populated sample due to the smaller area of COSMOS observed with the F125W, F140W, or F160W bands in the COSMOS-CANDELS subfield (0.05 sq deg.) region and the publicly available WFC3/IR coverage (∼0.05 sq deg.). For comparison, the low-redshift sample is derived from the full 1.7 sq deg. area covered by ACS. We note that the distribution of B/T ratios at high-z peaks at an intermediate type (B/T ∼ 0.5) due to the difficulty of modeling two morphological components at such a high redshift, even with HST images. Therefore, we highlight the results of the bulge- and disk-dominated samples. In Figure 12, we find that at high redshift ($z > 1$), the linearity of the SFMS strengthens with redshift as observed with the general population, however the larger error bars prevent a robust analysis of the turnover mass. Again, the SFMS estimated using each morphology bin are consistent with each other.

5. Discussion

5.1. Comparison to the Star Formation Main Sequence Literature

In Figure 7, we observe that our global star formation rate–stellar mass relations are consistent with the spread of previous SFMS results at low to intermediate masses. Our results are most consistent with Schreiber et al. (2015) once renormalized

to a Chabrier (2003) IMF. Our relations often indicate lower SFRs by 0.1–0.2 dex across stellar mass, but converge at higher stellar masses with other studies that observe a turnover (e.g., Whitaker et al. 2014; Schreiber et al. 2015). Two systematic effects are present that may be responsible for the offset in median SFR estimates. First, Schreiber et al. (2015) use a delayed exponentially declining star formation history while our MAGPHYS fits use a nondelayed exponentially declining star formation history. This delays the decline of SFR at high redshift in the models used in Schreiber et al. (2015), yielding a higher SFR than our sample fits until both reach a low SFR steady state at low redshift. Second, the choice of dust law may play a part in such an offset, as Schreiber et al. (2015) use the Calzetti et al. (2000) dust attenuation law while we use the Cunha et al. (2008) dust models included in MAGPHYS and SED3FIT that use a shallower slope, i.e., lower absorption for emission lines, for birth cloud attenuation (Salim & Narayanan 2020). Overall, our SFMS estimates are within the scatter of previous works on the SFMS, and consistent with the scatter about SFR and stellar mass estimates between SED-fitting codes identified in Pacifici et al. (2022).

The most similar to our SFMS fit, Schreiber et al.'s (2015) SFMS relation is calculated using galaxies selected from the GOODS-South (Guo et al. 2013), UltraDeep Survey (Galametz et al. 2013), and COSMOS-CANDELS fields (Nayyeri et al. 2017). Galaxies are selected above the i-, K-, or H-band completeness limit of each field. Similar to Whitaker et al. (2014), Schreiber et al. (2015) use the *UVJ* criteria of Williams et al. (2009) to select SF galaxies and estimate their star formation rates using the FAST package (Kriek et al. 2009). The FIR portion of their SEDs were constrained using median stacking of Herschel SPIRE observations. Schreiber et al.'s (2015) inclusion of NUV to FIR photometry in SED fitting, combined with a similar color–color based selection method, may explain our similar results.

In Figure 7 we plot the Whitaker et al. (2014) SFMS relation closest to the average redshift of each of our redshift bins. From $0.5 < z < 2.5$, Whitaker et al.'s (2014) results are often offset from this work's to higher SFRs. Their sample is selected from the five CANDELS fields, with stellar mass estimates calculated using the FAST stellar population fitting package (Kriek et al. 2009). However, their SFR estimates are calculated using two independent components for the unobscured and obscured SFRs. The bolometric IR (8–1000 μm) luminosity is calculated assuming the log average of the IR spectrum templates from Dale & Helou (2002). This total IR luminosity and the total integrated rest-frame luminosity at 1216–3000 Å are added and converted into a total SFR. The difference in SFRs between their results and ours may be due to the lack of an energy budget conservation, which constrains the height of the FIR peak in our fits and likewise constrains the SFRs estimated.

5.2. Implications of Environmental Effects

The lack of environmental dependence at high redshift seen in Figure 9 agrees with the recent literature, that finds no environmental dependence on the SFRs of galaxies on the main sequence at high redshift (Erfanianfar et al. 2015; Hatfield & Jarvis 2017; Leslie et al. 2020). Leslie et al. (2020) found no evidence for an environmental dependence of the SFMS out to $z \sim 3$ for a sample of galaxies selected with a comoving number density cut, as well as for X-ray groups out to $z \sim 0.75$,
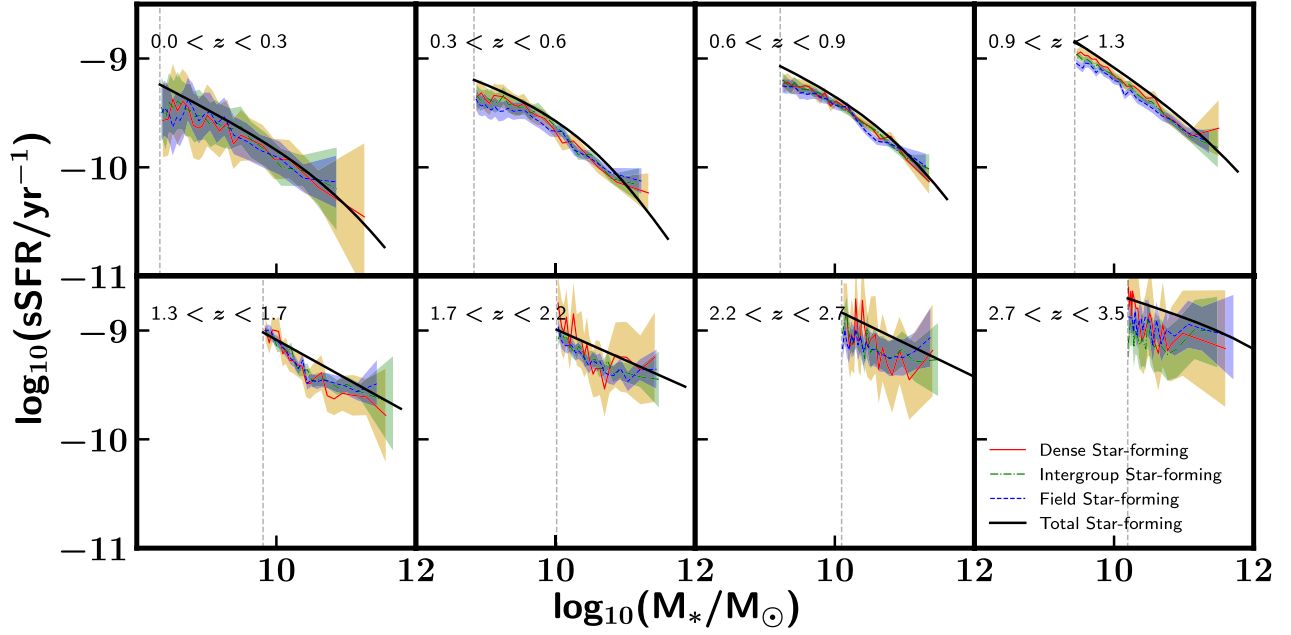
Figure 9. Our SFMS fit compared to the raw median specific star formation rate as a function of the stellar mass of star-forming (SF) galaxies in field ($\delta < \delta_{\mathrm{Median}}$, blue), intergroup ($\delta_{\mathrm{Median}} < \delta < 2 \times \delta_{\mathrm{Median}}$, green), and dense ($\delta > 2 \times \delta_{\mathrm{Median}}$, red) local environments. We find that SF galaxies in all environments are consistent within errors with our global SFMS and do not exhibit any environmental dependence with local environment at any stellar mass examined by our sample. The stellar mass completeness limit for each redshift bin is plotted with a vertical dashed line in black.
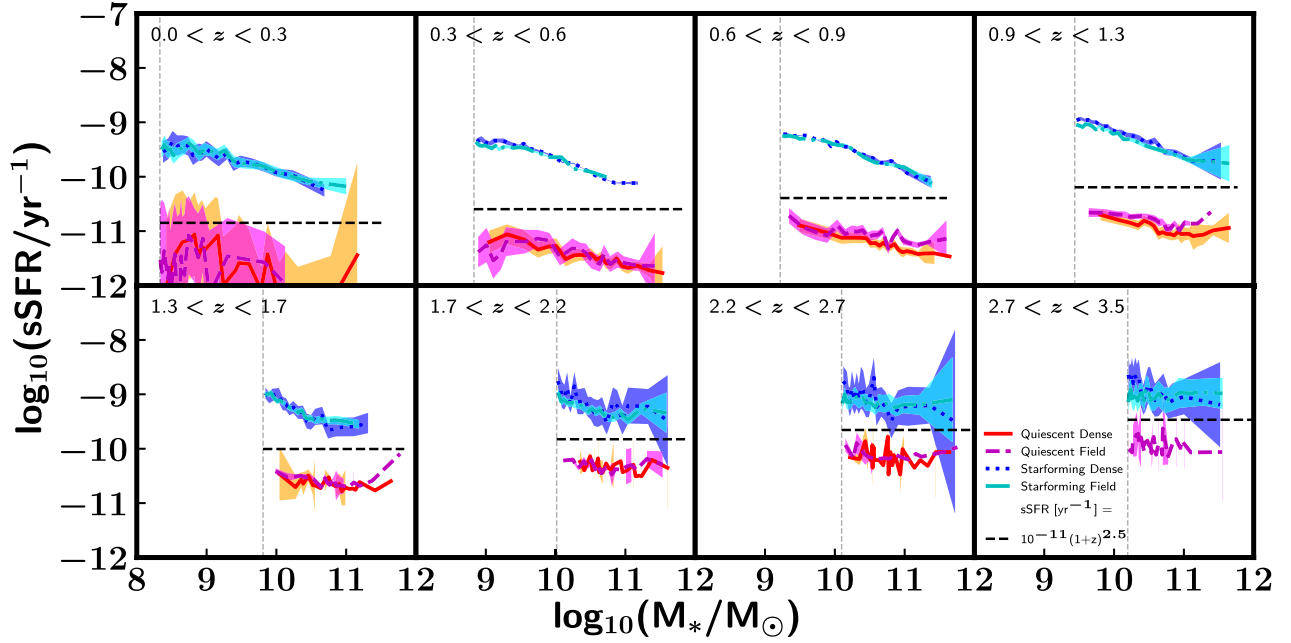
Figure 10. The median specific star formation rate in bins of 150 objects for galaxies in field ($\delta < \delta_{\mathrm{Median}}$, blue dashed), and dense ($\delta > 2\delta_{\mathrm{Median}}$, red solid) local environments. For this plot, we classify galaxies as star-forming (SF) based on NUVrJ colors only, and plot the sSFR cut used in the final sample selection process. At $z > 0.9$, we see that the SF and quiescent populations show no dependence on local environment. The SF populations in dense and field environments are consistent within errors of each other when a sSFR cut is used (see Figure 9). The stellar mass completeness limit for each redshift bin is plotted with a vertical dashed line in black.

using SFRs derived from 3 GHz radio continuum stacks. Recently, Randriamampandry et al. (2020) used the Very Large Array-COSMOS 3 GHz catalog to investigate groups using a friend-of-friends algorithm and likewise found no significant difference in SFR behavior as a function of environment at $z > 0.47$. Erfanianfar et al. (2015) also observed the effect of

local environment on the SFMS for galaxies in clusters and groups between $0.15 < z < 0.5$, and found galaxies in groups tended toward quiescence and also hosted a higher bulge-to-disk ratio than those in field or filament environments, consistent with Dressler's (1980) earlier findings that clusters hosted a greater frequency of ellipticals. They also identified a
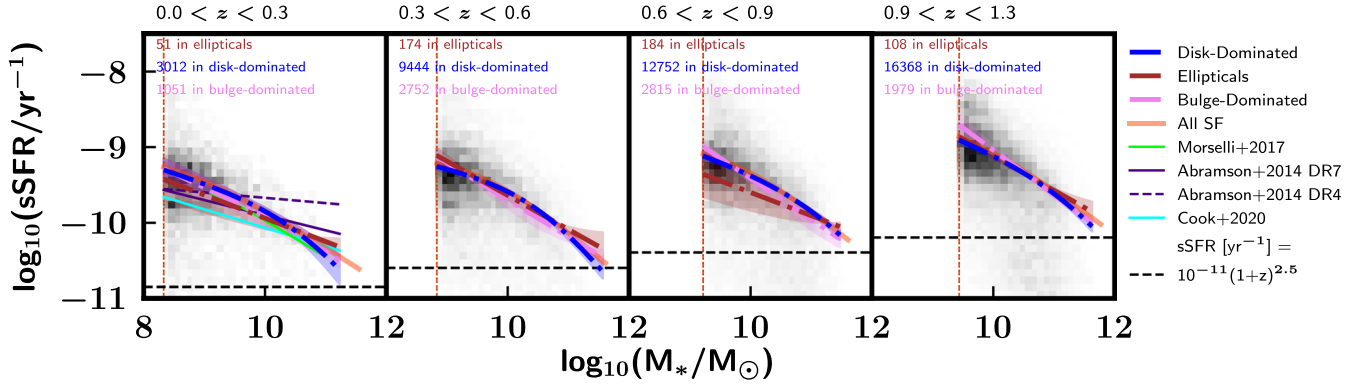
Figure 11. SFMS as estimated using only disk-dominated systems (BULG = 2 or 3, blue dashed–dotted), bulge-dominated disks (BULG = 0 or 1, magenta dashed–dotted), and elliptical systems (TYPE = 1, brown dashed–dotted) from the Zurich Structure & Morphology Catalog. Finally, we also include our global SFMS estimate in orange. We include the full sample as black density bins for reference. In the $z < 0.3$ subplot, we include literature from local studies such as the original Abramson et al. (2014) DR4 results showing a flat disk sSFR with mass (dashed violet) vs. the Abramson et al. (2014) DR7, Morselli et al. (2017), and Cook et al. (2020) results retaining a change in slope with stellar mass.
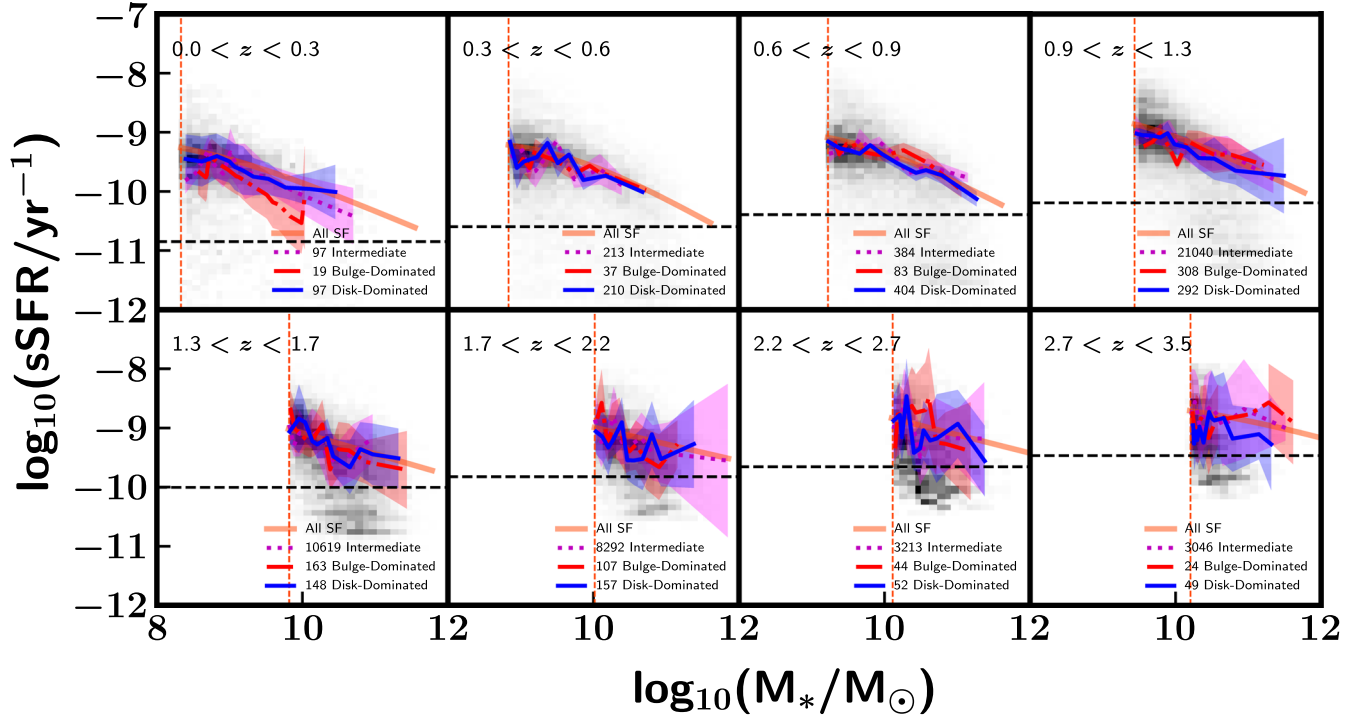
Figure 12. Median sSFR of disk-dominated (B/T < 0.25), bulge-dominated (B/T > 0.75), and intermediate (0.25 < B/T < 0.75) star-forming systems using GALAPAGOS-2 estimates derived from the CANDELS field and public HST WFC3/IR archival data. Each sample is plotted in 30 stellar mass bins. Star-forming galaxies are selected using a NUVrJ color–color criteria and sSFR cut (black dashed line) of $>10^{-11}(1+z)^{2.5}$ yr^{-1}, as described in Section 4, and we include our global SFMS estimate in orange for reference. Star-forming galaxies from the disk-dominated bin are in blue solid lines and from the bulge-dominated bin in red dashed–dotted lines, with intermediates as magenta dotted. We include the full sample for reference as a black two-dimensonal histogram. We no longer find the turnover in our morphology-selected SFMS estimates at $z > 1.3$, however the errors on the median are too large to determine any difference as a function of B/T ratio.

similar cutoff in stellar mass $10^{10.4}$–$10^{10.6}$ $M_\odot$, above which the SFMS flattens and no longer increases in SFR with stellar mass.

Erfanianfar et al.'s (2015) sample is drawn from the X-ray groups observed in the ECDFS, CDFN, AEGIS, and COSMOS X-ray surveys (Finoguenov et al. 2007), selecting groups with halo masses $10^{12.5}$–$10^{14.3}$ $M_\odot$. This differs from our local density field estimation method, which classifies density in relation to the median density at a given redshift. However, the majority of their group sample lies in environments with a density >2 times the comoving density of their overall galaxy

sample, indicating a similarity between their "group" environment and our "dense" environment classifications. This consistency in environmental measurements may play a part in SFMS environmental results, indicating that massive, dense environments at low redshift support quenching more efficiently than the lower mass halos and environments available at high redshift ($z > 0.9$). Overall, our results provide a self-consistent estimation of the SFMS across a wide dynamic range of redshift, connecting the individual results of low- and high-z studies into a connected picture that refutes the need for an environmental dependence.

Looking at the quiescent population in Figure 10, we compare the median SFRs of both star-forming and quiescent galaxies to examine whether we observe any difference in the SFR of the quiescent sample as a function of environment. Similar to the star-forming sample, we see little difference between each quiescent subsample. The consistent SFRs of NUVrJ star-forming or quiescent samples across extreme environments support the model that quenching is a fast process (<billion year timescale) that quickly transfers star-forming galaxies to the quiescent population once cluster-specific quenching begins to take effect.

5.3. Interplay of Morphology and Environment

In Figure 11, we show that disk-dominated star-forming galaxies at low redshift experience a consistent decline with stellar mass in the same way as the overall SF galaxy population and bulge-dominated galaxies (Figure 7). This consistency indicates that the sSFRs of disks in massive SF galaxies begin to experience a decline in star formation with stellar mass at $z < 1.3$ and that star formation activity per stellar mass bin is insensitive to the bulge fraction. Our estimates are consistent with works that used photometry-based SED fitting to estimate SFR and stellar masses (Schreiber et al. 2016; Catalán-Torrecilla et al. 2017; Morselli et al. 2017; Belfiore et al. 2018; Cook et al. 2020).

In contrast, the papers that inspired our work here found a roughly constant evolution of sSFR with disk stellar mass (Abramson et al. 2014; Guo et al. 2015), i.e., a lack of turnover (Popesso et al. 2019). The Abramson et al. (2014) sample was derived from the SDSS Data Releases 4 (DR4) and 7 (DR7), and has a median $z \sim 0.08$. The Abramson et al. (2014) B/T ratios were estimated using a two-component fit of face-on disks and a B/T cutoff of 0.2. However, one key difference is the use of SFRs from Brinchmann et al. (2004), who use SDSS optical emission lines and classify a galaxy as star-forming only if all four Baldwin–Phillips–Telervich diagram lines are detected. As shown in Figure 11, Abramson et al. (2014) used the SFRs from both SDSS DR4 and 7, with the flattest relation being derived from SDSS DR4. DR4 spectral-line-derived SFRs are warned as erroneously high for quiescent galaxies, and this is observed to drive SFRs toward higher values at the high-mass, low-SFR end of the star-forming population. Leslie et al. (2020) also used SF galaxies in COSMOS and used the Zurich catalog to classify disk-dominated galaxies, but did not observe any turnover. This is due to a lack of disk-dominated SF galaxies in their sample above $10^{11}\ M_\odot$, where our analysis most strongly observed a decline in sSFR with stellar mass.

Morselli et al. (2017) examined disks in a low-z sample from $0.02 < z < 0.1$ using a decomposition of SDSS optical images and SFRs from optical emission lines. They found that low-z disk SFRs weakly flatten with stellar mass, and can also be correlated linearly within the errors. Also at low z, Cook et al. (2020) used the GALEX Arecibo SDSS Survey to examine the SFRS of disks using a combined NUV+MIR measurement alongside SDSS gri band images, but found a decline in SFR with mass when bulges were removed.

Building out to intermediate redshift, Erfanianfar et al. (2015) conducted a similar investigation examining the offset from the SFMS for SF galaxies across COSMOS, AEGIS, ECDFS, and CDFN at $z < 1.1$. Across local environments, they found a turnover at $10^{10.5}\ M_\odot$ but also observed an offset between high and low Sérsic systems at high stellar masses.

Figure 12 extends the redshift range for which combined morphology and environment studies have estimated the SFMS out to $z < 3$, agreeing with local optical studies that disks and disk-dominated systems experience a turnover at high stellar mass up to $z < 1.3$. Previous works such as Lee et al. (2018) relied on single Sérsic profile fits to determine morphology at high z, so cannot be directly compared to our results. However, Lee et al. (2018) also found a flattening of the SFMS at high mass for their low-bulge ($n < 1.5$) systems, roughly consistent with our conclusions. Once at $z > 1.3$, we find the sSFRs of SF galaxies in general, as well as disk-dominated SF galaxies, follows a linear relation that is insensitive to bulge fraction. This provides new evidence strengthening the case for a consistently declining specific star formation with stellar mass in SF galaxies regardless of bulge fraction.

6. Conclusions

We investigate how the star formation rate–stellar mass relation evolves with morphology and environment for both the total population and disk-dominated systems. This is one of the first studies to comprehensively and consistently investigate the evolution of the SFMS as a function of both environment and morphology over such a large fraction of cosmic time ($0 < z < 3.5$). Our methods enable consistent treatment of environment across our redshift range. To address morphology, we use morphology catalogs across two wavelength regimes to measure the rest-frame optical; care must be taken to compare either low- or high-z morphology samples to works at other redshifts. We estimate SFRs and stellar masses using SED fitting of a stellar mass complete sample from the COS-MOS2015 catalog (Laigle et al. 2016). We consider local environment using the weighted adaptive kernel smoothed maps of the COSMOS field (Darvish et al. 2015), which provide a unique opportunity to discover which morphology populations are driving the previously observed evolution of the SFMS with redshift (Whitaker et al. 2012, 2014; Lee et al. 2015). From our investigation, we identify several key results that provide greater context to our knowledge of the SFMS:

1. A dependence of the SFMS with environment is not observed when either a NUVrJ color–color selection or a combined NUVrJ and sSFR selection function is used to select the star-forming sample. The median star formation rates of SF and quiescent galaxies are respectively consistent between their environment bins in all redshift bins.

2. We observe that the turnover of the SFMS when considering disk-dominated (B/T < 0.25) systems is consistent with the global trend as well as more bulge-dominated systems. This implies that the turnover is due at least in part to a change in sSFR within the disk components and not driven by the transition from disk-dominated to bulge-dominated systems. We also identify a potential cause of disagreements in the literature, as our work supports previous studies based on multiple photometric bands in the SFR estimates. The flattening of the SFMS may be a feature that requires the ability to identify only moderately SF galaxies at the high-mass end in addition to starbursts.

From our results in Figure 10, we find that the color–color-selected SF galaxies residing in dense environments host median SFRs and errors consistent with their equal-mass

partners in field environments. As the density maps used in this study estimate the local environment in the COSMOS field as a function of the median density in a given redshift slice, future studies may build upon these results by also investigating the absolute mass of cluster and protoclusters to confirm whether the environmental effects we observe here are a function of absolute total mass or the increasing dynamic range of environmental densities at low redshift.

When considering these results, we assemble a picture of how similar SF galaxies evolve over cosmic time. At high redshift, galaxies at all stellar masses are forming stars at a rate that is an order of magnitude or more greater than observed at present day. The most massive galaxies in the universe during this high-redshift epoch form stars with a similar sSFR as lower mass galaxies.

From $z \sim 1.3$ to the present day, the most massive galaxies undergo a decline in SFR in comparison to low- and intermediate-mass galaxies at the same redshift. This is evidence of the process of galactic "downsizing," where the most massive galaxies conclude their star-formation-dominated evolutionary eras first. When considering only disk-dominated systems, we still observe this trend. This indicates an evolution in specific star formation is experienced by all morphological components with mass, with higher mass bulge- and disk-dominated systems both experiencing a decline in sSFR.

ORCID iDs

Kevin C. Cooke https://orcid.org/0000-0002-2200-9845
Jeyhan S. Kartaltepe https://orcid.org/0000-0001-9187-3605
Caitlin Rose https://orcid.org/0000-0002-8018-3219
Behnam Darvish https://orcid.org/0000-0003-4919-9017
Sarah K. Leslie https://orcid.org/0000-0002-4826-8642
Anton M. Koekemoer https://orcid.org/0000-0002-6610-2048

References

Abramson, L. E., Kelson, D. D., Dressler, A., et al. 2014, ApJ, 785, L36
Alberts, S., Pope, A., Brodwin, M., et al. 2016, ApJ, 825, 72
Arnouts, S., Cristiani, S., Moscardini, L., et al. 1999, MNRAS, 310, 540
Arnouts, S., Walcher, C. J., Le Fèvre, O., et al. 2007, A&A, 476, 137
Aune, S., Boulade, O., Charlot, X., et al. 2003, Proc. SPIE, 4841, 513
Baldry, I. K., Balogh, M. L., Bower, R. G., et al. 2006, MNRAS, 373, 469
Baldry, I. K., Glazebrook, K., Brinkmann, J., et al. 2004, ApJ, 600, 681
Balogh, M. L., McGee, S. L., Wilman, D. J., et al. 2011, MNRAS, 412, 2303
Barden, M., Häußler, B., Peng, C. Y., McIntosh, D. H., & Guo, Y. 2012, MNRAS, 422, 449
Belfiore, F., Maiolino, R., Bundy, K., et al. 2018, MNRAS, 477, 3014
Berta, S., Lutz, D., Santini, P., et al. 2013, A&A, 551, A100

Boulade, O., Charlot, X., Abbon, P., et al. 2003, Proc. SPIE, 4841, 72
Brammer, G. B., van Dokkum, P. G., Franx, M., et al. 2012, ApJS, 200, 13
Brinchmann, J., Charlot, S., White, S. D. M., et al. 2004, MNRAS, 351, 1151
Bruzual, G., & Charlot, S. 2003, MNRAS, 344, 1000
Calzetti, D., Armus, L., Bohlin, R. C., et al. 2000, ApJ, 533, 682
Capak, P., Aussel, H., Ajiki, M., et al. 2007, ApJS, 172, 99
Capak, P., Mobasher, B., Scoville, N. Z., et al. 2011, ApJ, 730, 68
Casey, C. M., Chen, C.-C., Cowie, L. L., et al. 2013, MNRAS, 436, 1919
Casey, C. M., Cooray, A., Killi, M., et al. 2017, ApJ, 840, 101
Catalán-Torrecilla, C., Gil de Paz, A., Castillo-Morales, A., et al. 2017, ApJ, 848, 87
Chabrier, G. 2003, PASP, 115, 763
Chauke, P., van der Wel, A., Pacifici, C., et al. 2019, ApJ, 877, 48
Colless, M., Dalton, G., Maddox, S., et al. 2001, MNRAS, 328, 1039
Cook, R. H. W., Cortese, L., Catinella, B., & Robotham, A. 2020, MNRAS, 493, 5596
Cooke, K. C., Kartaltepe, J. S., Tyler, K. D., et al. 2019, ApJ, 881, 150
Cooke, K. C., Kirkpatrick, A., Estrada, M., et al. 2020, ApJ, 903, 106
Cooper, M. C., Newman, J. A., Weiner, B. J., et al. 2008, MNRAS, 383, 1058
da Cunha, E., Charlot, S., & Elbaz, D. 2008, MNRAS, 388, 1595
Daddi, E., Dickinson, M., Morrison, G., et al. 2007, ApJ, 670, 156
Dale, D. A., & Helou, G. 2002, ApJ, 576, 159
Darvish, B., Mobasher, B., Sobral, D., Scoville, N., & Aragon-Calvo, M. 2015, ApJ, 805, 121
Darvish, B., Sobral, D., Mobasher, B., et al. 2014, ApJ, 796, 51
Davidzon, I., Ilbert, O., Laigle, C., et al. 2017, A&A, 605, A70
Domínguez Sánchez, H., Pozzi, F., Gruppioni, C., et al. 2011, MNRAS, 417, 900
Dressler, A. 1980, ApJ, 236, 351
Elbaz, D., Daddi, E., Le Borgne, D., et al. 2007, A&A, 468, 33
Elbaz, D., Dickinson, M., Hwang, H. S., et al. 2011, A&A, 533, A119
Ellison, S. L., Lin, L., Thorp, M. D., et al. 2021, MNRAS, 501, 4777
Erfanianfar, G., Popesso, P., Finoguenov, A., et al. 2015, MNRAS, 455, 2839
Fazio, G. G., Hora, J. L., Allen, L. E., et al. 2004, ApJS, 154, 10
Feltre, A., Hatziminaoglou, E., Fritz, J., & Franceschini, A. 2012, MNRAS, 426, 120
Feruglio, C., Aussel, H., Le Floc'h, E., et al. 2010, ApJ, 721, 607
Finoguenov, A., Guzzo, L., Hasinger, G., et al. 2007, ApJS, 172, 182
Fu, H., Yan, L., Scoville, N. Z., et al. 2010, ApJ, 722, 653
Galametz, A., Grazian, A., Fontana, A., et al. 2013, ApJS, 206, 10
Genzel, R., Tacconi, L. J., Lutz, D., et al. 2015, ApJ, 800, 20
George, M. R., Leauthaud, A., Bundy, K., et al. 2011, ApJ, 742, 125
Gobat, R., Strazzullo, V., Daddi, E., et al. 2013, ApJ, 776, 9
Griffin, M. J., Abergel, A., Abreu, A., et al. 2010, A&A, 518, L3
Grogin, N. A., Kocevski, D. D., Faber, S. M., et al. 2011, ApJS, 197, 35
Gunn, J. E., Gott, J., & Richard, I. 1972, ApJ, 176, 1
Guo, K., Zheng, X. Z., Wang, T., & Fu, H. 2015, ApJ, 808, L49
Guo, Y., Ferguson, H. C., Giavalisco, M., et al. 2013, ApJS, 207, 24
Hashemizadeh, A., Driver, S. P., Davies, L. J. M., et al. 2021, MNRAS, 505, 136
Hasinger, G., Capak, P., Salvato, M., et al. 2018, ApJ, 858, 77
Hatfield, P. W., & Jarvis, M. J. 2017, MNRAS, 472, 3570
Häußler, B., Bamford, S. P., Vika, M., et al. 2013, MNRAS, 430, 330
Häußler, B., Vika, M., Bamford, S. P., et al. 2022, A&A, 664, A92
Hilton, M., Lloyd-Davies, E., Stanford, S. A., et al. 2010, ApJ, 718, 133
Hung, C.-L., Sanders, D. B., Casey, C. M., et al. 2013, ApJ, 778, 129
Hunter, J. D. 2007, CSE, 9, 90
Ilbert, O., Arnouts, S., McCracken, H. J., et al. 2006, A&A, 457, 841
Ilbert, O., Salvato, M., Le Floc'h, E., et al. 2010, ApJ, 709, 644
Ilbert, O., McCracken, H. J., Le Fevre, O., et al. 2013, A&A, 556, A55
Johnston, R., Vaccari, M., Jarvis, M., et al. 2015, MNRAS, 453, 2541
Karim, A., Schinnerer, E., Martínez-Sansigre, A., et al. 2011, ApJ, 730, 61
Kartaltepe, J. S., Sanders, D. B., Le Floc'h, E., et al. 2010, ApJ, 709, 572
Kartaltepe, J. S., Dickinson, M., Alexander, D. M., et al. 2012, ApJ, 757, 23
Kartaltepe, J. S., Mozena, M., Kocevski, D., et al. 2015, ApJ, 221, 11
Kaviraj, S., Peirani, S., Khochfar, S., Silk, J., & Kay, S. 2009, MNRAS, 394, 1713
Kennedy, R., Bamford, S. P., Häußler, B., et al. 2016, MNRAS, 460, 3458
Koekemoer, A. M., Aussel, H., Calzetti, D., et al. 2007, ApJS, 172, 196
Koekemoer, A. M., Faber, S. M., Ferguson, H. C., et al. 2011, ApJS, 197, 36
Koyama, Y., Smail, I., Kurk, J., et al. 2013, MNRAS, 434, 423
Kriek, M., van Dokkum, P. G., Labbé, I., et al. 2009, ApJ, 700, 221
Kriek, M., van Dokkum, P. G., Franx, M., et al. 2006, ApJL, 649, L71
Kriek, M., Shapley, A. E., Reddy, N. A., et al. 2015, ApJS, 218, 15
Krogager, J.-K., Zirm, A. W., Toft, S., Man, A., & Brammer, G. 2014, ApJ, 797, 17

Laigle, C., McCracken, H. J., Ilbert, O., et al. 2016, ApJS, 224, 24
Le Fèvre, O., Tasca, L. A. M., Cassata, P., et al. 2015, A&A, 576, A79
Lee, B., Giavalisco, M., Whitaker, K., et al. 2018, ApJ, 853, 131
Lee, N., Le Floc'h, E., Sanders, D. B., et al. 2010, ApJ, 717, 175
Lee, N., Sanders, D. B., Casey, C. M., et al. 2015, ApJ, 801, 80
Leslie, S. K., Schinnerer, E., Liu, D., et al. 2020, ApJ, 899, 58
Lilly, S. J., Fevre, O. L., Renzini, A., et al. 2007, ApJS, 172, 70
Lin, L., Jian, H.-Y., Foucaud, S., et al. 2014, ApJ, 782, 33
Liu, D., Lang, P., Magnelli, B., et al. 2019, ApJS, 244, 40
Lutz, D., Poglitsch, A., Altieri, B., et al. 2011, A&A, 532, A90
Madau, P., & Dickinson, M. 2014, ARA&A, 52, 415
Magdis, G. E., Elbaz, D., Daddi, E., et al. 2010, ApJ, 714, 1740
Magdis, G. E., Daddi, E., Béthermin, M., et al. 2012, ApJ, 760, 6
Mancini, C., Daddi, E., Juneau, S., et al. 2019, in The Art of Measuring Galaxy Physical Properties, 49, https://app.iasf-milano.inaf.it
Martin, D. C., Fanson, J., Schiminovich, D., et al. 2005, ApJL, 619, L1
Masters, D. C., Stern, D. K., Cohen, J. G., et al. 2017, ApJ, 841, 111
McCracken, H. J., Milvang-Jensen, B., Dunlop, J., et al. 2012, A&A, 544, A156
Mobasher, B. 2016, Spectroscopic Properties of Galaxies in the Cosmic Web, Keck Observatory Archive, U200D
Molnár, D. C., Sargent, M. T., Delhaize, J., et al. 2018, MNRAS, 475, 827
Momcheva, I. G., Brammer, G. B., van Dokkum, P. G., et al. 2016, ApJS, 225, 27
Morrissey, P., Conrow, T., Barlow, T. A., et al. 2007, ApJS, 173, 682
Morselli, L., Popesso, P., Cibinel, A., et al. 2019, A&A, 626, A61
Morselli, L., Popesso, P., Erfanianfar, G., & Concas, A. 2017, A&A, 597, A97
Mowla, L. A., van Dokkum, P., Brammer, G. B., et al. 2019, ApJ, 880, 57
Nanayakkara, T., Glazebrook, K., Kacprzak, G. G., et al. 2016, ApJ, 828, 21
Nayyeri, H., Hemmati, S., Mobasher, B., et al. 2017, ApJS, 228, 7
Noeske, K. G., Faber, S. M., Weiner, B. J., et al. 2007, ApJL, 660, L47
Oke, J. B. 1974, ApJS, 27, 21
Oliver, S. J., Bock, J., Altieri, B., et al. 2012, MNRAS, 424, 1614
Pacifici, C., Iyer, K. G., Mobasher, B., et al. 2022, ApJ, in press, arXiv:2212.01915
Pannella, M., Carilli, C. L., Daddi, E., et al. 2009, ApJL, 698, L116
Pâris, I., Petitjean, P., Aubourg, É, et al. 2018, A&A, 613, A51
Pearson, W. J., Wang, L., Hurley, P. D., et al. 2018, A&A, 615, A146
Peng, C. Y., Ho, L. C., Impey, C. D., & Rix, H.-W. 2002, AJ, 124, 266
Peng, C. Y., Ho, L. C., Impey, C. D., & Rix, H.-W. 2010, AJ, 139, 2097
Perez, F., & Granger, B. E. 2007, CSE, 9, 21
Perna, M., Brusa, M., Salvato, M., et al. 2015, A&A, 583, A72
Pilbratt, G. L., Riedinger, J. R., Passvogel, T., et al. 2010, A&A, 518, L1
Poglitsch, A., Waelkens, C., Geis, N., et al. 2010, A&A, 518, L2
Popesso, P., Morselli, L., Concas, A., et al. 2019, MNRAS, 490, 5285
Price-Whelan, A. M., Sipőcz, B. M., Günther, H. M., et al. 2018, AJ, 156, 123
Randriamampandry, S. M., Vaccari, M., & Hess, K. M. 2020, MNRAS, 499, 948
Robitaille, T. P., Tollerud, E. J., Greenfield, P., et al. 2013, A&A, 558, A33
Rochester Institute of Technology 2019, Research Computing Services, doi:10.34788/0S3G-QD15
Rodighiero, G., Cimatti, A., Gruppioni, C., et al. 2010, A&A, 518, L25
Rodighiero, G., Renzini, A., Daddi, E., et al. 2014, MNRAS, 443, 19
Salim, S., & Narayanan, D. 2020, ARA&A, 58, 529
Salim, S., Rich, R. M., Charlot, S., et al. 2007, ApJS, 173, 267
Sanders, D. B., Salvato, M., Aussel, H., et al. 2007, ApJS, 172, 86
Santos, J. S., Altieri, B., Tanaka, M., et al. 2014, MNRAS, 438, 2565
Sargent, M. T., Carollo, C. M., Lilly, S. J., et al. 2007, ApJS, 172, 434
Scarlata, C., Carollo, C. M., Lilly, S., et al. 2007, ApJS, 172, 406
Schinnerer, E., Groves, B., Sargent, M. T., et al. 2016, ApJ, 833, 112
Schlegel, D. J., Finkbeiner, D. P., & Davis, M. 1998, ApJ, 500, 525
Schreiber, C., Elbaz, D., Pannella, M., et al. 2016, A&A, 589, A35
Schreiber, C., Pannella, M., Elbaz, D., et al. 2015, A&A, 575, A74
Scott, K. S., Austermann, J. E., Perera, T. A., et al. 2008, MNRAS, 385, 2225
Scoville, N., Aussel, H., Brusa, M., et al. 2007, ApJS, 172, 1
Scoville, N., Arnouts, S., Aussel, H., et al. 2013, ApJS, 206, 3
Scoville, N., Sheth, K., Aussel, H., et al. 2016, ApJ, 820, 83
Silverman, J. D., Kashino, D., Sanders, D., et al. 2015, ApJS, 220, 12
Speagle, J. S., Steinhardt, C. L., Capak, P. L., & Silverman, J. D. 2014, ApJS, 214, 15
Steinhardt, C. L., Speagle, J. S., Capak, P., et al. 2014, ApJL, 791, L25
Strateva, I., Ivezić, Ž, Knapp, G. R., et al. 2001, AJ, 122, 1861
Sutherland, W., Emerson, J., Dalton, G., et al. 2015, A&A, 575, A25
Taniguchi, Y., Scoville, N., Murayama, T., et al. 2007, ApJS, 172, 9
Taniguchi, Y., Kajisawa, M., Kobayashi, M. A. R., et al. 2015, PASJ, 67, 104

Tempel, E., Kipper, R., Saar, E., et al. 2014, A&A, 572, A8
Thorne, J. E., Robotham, A. S. G., Davies, L. J. M., et al. 2021, MNRAS, 505, 540
Toft, S., Franx, M., van Dokkum, P., et al. 2009, ApJ, 705, 255
Toft, S., van Dokkum, P., Franx, M., et al. 2007, ApJ, 671, 285
Tomczak, A. R., Quadri, R. F., Tran, K.-V. H., et al. 2016, ApJ, 817, 118
Trakhtenbrot, B., Civano, F., Urry, C. M., et al. 2016, ApJ, 825, 4
Trump, J. R., Impey, C. D., McCarthy, P. J., et al. 2007, ApJS, 172, 383
Trump, J. R., Impey, C. D., Elvis, M., et al. 2009, ApJ, 696, 1195
Trump, J. R., Nagao, T., Ikeda, H., et al. 2011, ApJ, 732, 23
van der Walt, S., Colbert, S. C., & Varoquaux, G. 2011, CSE, 13, 22
van der Wel, A., Noeske, K., Bezanson, R., et al. 2016, ApJS, 223, 29
Virtanen, P., Gommers, R., Oliphant, T. E., et al. 2020, NatMe, 17, 261

Werner, M. W., Roellig, T. L., Low, F. J., et al. 2004, ApJS, 154, 1
Whitaker, K. E., van Dokkum, P. G., Brammer, G., & Franx, M. 2012, ApJL, 754, L29
Whitaker, K. E., Franx, M., Leja, J., et al. 2014, ApJ, 795, 104
Willett, K. W., Schawinski, K., Simmons, B. D., et al. 2015, MNRAS, 449, 820
Williams, R. J., Quadri, R. F., Franx, M., van Dokkum, P., & Labbé, I. 2009, ApJ, 691, 1879
Wisnioski, E., Förster Schreiber, N. M., Wuyts, S., et al. 2015, ApJ, 799, 209
Wuyts, S., Förster Schreiber, N. M., van der Wel, A., et al. 2011, ApJ, 742, 96
Yoshikawa, T., Akiyama, M., Kajisawa, M., et al. 2010, ApJ, 718, 112
Zamojski, M. A., Schiminovich, D., Rich, R. M., et al. 2007, ApJS, 172, 468